

Review

A Review of the Mineral Chemistry and Crystallization Conditions of Ediacaran–Cambrian A-Type Granites in the Central Subprovince of the Borborema Province, Northeastern Brazil

Jefferson Valdemiro de Lima ^{1,*}, Iñez de Pinho Guimarães ², José Victor Antunes de Amorim ³ , Caio Cezar Garnier Brainer ², Lucilene dos Santos ⁴  and Adejardo Francisco da Silva Filho ²

¹ Faculdade de Geologia, Universidade Federal do Sul e Sudeste do Pará, Marabá 68500-000, PA, Brazil

² Programa de Pós-Graduação em Geociências, Universidade Federal de Pernambuco, Recife 50740-540, PE, Brazil; ignezdpg@gmail.com (I.d.P.G.); caiocgbrainer@gmail.com (C.C.G.B.); afsf56@gmail.com (A.F.d.S.F.)

³ School of Earth Sciences, The University of Western Australia, Perth, WA 6009, Australia; josevictor.antunesdeamorim@research.uwa.edu.au

⁴ Departamento de Geologia, Universidade Federal do Ceará, Fortaleza 60355-636, CE, Brazil; lucilene.santos01@gmail.com

* Correspondence: jefferson1901@gmail.com or jefferson.valdemiro@unifesspa.edu.br; Tel.: +55-81-982170432

Abstract: Ediacaran–Cambrian magmatism in the Central Subprovince (Borborema Province, NE Brazil) generated abundant A-type granites. This study reviews published whole-rock and mineral chemistry data from thirteen Ediacaran–Cambrian A-type intrusions and a related dike swarm. It also presents new mineral chemistry and whole-rock data for one of these intrusions, along with zircon trace element data for five of the intrusions. Geochronological data from the literature indicate the formation of these A-type intrusions during a 55 Myr interval (580–525 Ma), succeeding the post-collisional high-K magmatism in the region at c. 590–580 Ma. The studied plutons intruded Paleoproterozoic basement gneisses or Neoproterozoic supracrustal rocks. They are ferroan, metaluminous to peraluminous and mostly alkalic–calcic. The crystallization parameters show pressure estimates mainly from 4 to 7 kbar, corresponding to crustal depths of 12 to 21 km, and temperatures ranging from 1160 to 650 °C in granitoids containing mafic enclaves, and from 990 to 680 °C in those lacking or containing only rare mafic enclaves. The presence of Fe-rich mineral assemblages including ilmenite indicates that the A-type granites crystallized under low fO_2 conditions. Zircon trace element analyses suggest post-magmatic hydrothermal processes, interpreted to be associated with shear zone reactivation. Whole-rock geochemical characteristics, the chemistry of the Fe-rich mafic mineral assemblages, and zircon trace elements in the studied granitoids share important similarities with A₂-type granites worldwide.

Keywords: A-type granite; post-collisional; Borborema Province



Citation: de Lima, J.V.; Guimarães, I.d.P.; de Amorim, J.V.A.; Brainer, C.C.G.; dos Santos, L.; da Silva Filho, A.F. A Review of the Mineral Chemistry and Crystallization Conditions of Ediacaran–Cambrian A-Type Granites in the Central Subprovince of the Borborema Province, Northeastern Brazil. *Minerals* **2024**, *14*, 1022. <https://doi.org/10.3390/min14101022>

Academic Editor: Clemente Recio

Received: 2 September 2024

Revised: 6 October 2024

Accepted: 8 October 2024

Published: 11 October 2024



Copyright: © 2024 by the authors. Licensee MDPI, Basel, Switzerland. This article is an open access article distributed under the terms and conditions of the Creative Commons Attribution (CC BY) license (<https://creativecommons.org/licenses/by/4.0/>).

1. Introduction

Granitic magmatism is essential for continental crust differentiation [1–4]. The origin of granitic magmas is either explained by fractionation of mantle-derived magmas, partial melting of different crustal lithologies induced by mantle heat flow, or the mixing of mantle- and crust-derived melts [5–9]. Heat transfer, as hot magmas ascend through the continental crust, may result in additional partial melting processes and the incorporation of the surrounding rocks, increasing the chemical and petrological complexity of granitic rocks [10–13]. Granites are widespread worldwide and have intruded into the Earth's crust throughout all geologic periods, in a manner associated with several geodynamic processes [14–17]. Despite their relatively simple mineralogy, granites commonly show a

wide array of modal and chemical compositions, reflecting the different processes associated with their emplacement and genesis [18–20].

The term A-type granite was introduced to define a specific group of iron-enriched granites with alkaline affinities, characterized by an anhydrous mineral assemblage, formed under low oxygen fugacity (fO_2) conditions, interpreted as intruded in an anorogenic tectonic setting [21]. However, since this definition, studies have shown that A-type plutons have a broader compositional range and may form in many tectonic settings, which has sparked a long-standing debate about their genesis and tectonic significance [22–33].

Overall, the mineral assemblage of A-type granites is composed of iron-rich (e.g., annite, siderophyllite, Fe-hedenbergite, Fe-hastingsite, fayalite) and/or alkali-rich (e.g., aegirine, arfvedsonite, and riebeckite) mafic silicates, associated with perthitic feldspars [18,23,28]. Geochemically, A-type rocks have high total alkalis ($K_2O + Na_2O$); high field strength (HFS) and rare earth element (REE) contents; high Fe# [$FeOt/(FeOt + MgO)$] values; and low MgO, CaO, Eu, and Sr contents [22,23,31].

In contrast with the initially proposed anorogenic origin [21], most studies indicate that A-type granites are emplaced in a variety of environments, both in post-collisional (e.g., orogenic collapse, strike-slip shear zones) and extensional settings (e.g., within-plate, rift, back-arc) [23,32,34]. Although it is generally accepted that A-type granites crystallize at higher temperatures and under more reducing conditions than other types of granite, the sources and crystallization conditions for A-type granite formation are also debatable [22,27,29]. Three main processes have been proposed to produce most A-type compositions, as summarized by Frost and Frost [22]: extreme differentiation from a basaltic source (with incremental degrees of crustal assimilation), partial melting of tonalitic–granitic crust, or a combination of the previous two processes.

In the Borborema Province of NE Brazil, abundant Ediacaran–Cambrian A-type granites have been reported in the Central Subprovince [35–40]. These granites are essential for understanding the multiple episodes of post-collisional deformation during the final stages of the Brasiliano Orogeny and its Pan-African counterparts [35,37,40]. Furthermore, the expressive A-type magmatism in the region provides valuable insights into the processes and conditions associated with A-type granites.

In this study, we review the mineral chemistry and whole-rock data of 13 A-type granitic plutons and a related dike swarm in the Central Subprovince of the Borborema Province, NE Brazil. Most of the data were compiled from scientific articles, but unpublished data, including those obtained from academic works (dissertations and theses), were also included. Additionally, we present new zircon trace element data for five of these granitic intrusions. The aim is to contribute to the discussion and enhance knowledge of the magmatic processes involved in the genesis of A-type granites and provide new insights into the geodynamic evolution of the later stages of the Brasiliano–Pan-African Orogeny in the Borborema Province.

2. The Borborema Province Geological Background

The Borborema Province (BP), located in northeastern Brazil, is limited to the north, the east, and the west by Phanerozoic sedimentary basins, and to the south by the São Francisco Craton. The BP (Figure 1A) is an orogenic belt formerly located in the northwestern–central part of West Gondwana, formed via the convergence and collision of the West Africa, Congo–São Francisco, and Amazonia Cratons during the Cryogenian–Ediacaran (c. 600–630 Ma), in an event known as the Brasiliano–Pan-African Orogeny [41–44].

The BP is divided by the large E-trending Patos and Pernambuco shear zones into three subprovinces (Figure 1B), i.e., North, Central, and South, and each subprovince is subdivided into tectonic domains [43,45]. The studied intrusions are located in the Central Subprovince (Figure 1B).

Overall, the geology of the Borborema Province can be summarized into Paleoproterozoic gneiss–migmatite basement complexes (c. 1.98–2.20 Ga) with Archean nuclei [45–48]; partly overlain by Neoproterozoic metasedimentary–metavolcanic supracrustal sequences [49–53];

intruded by widespread Neoproterozoic predominantly granitic magmatism [54–60]; and cut or bounded by large transcurrent shear zones trending NE or E, with possible continuation into the African continent [61–65].

The first stages of the Neoproterozoic tectonic evolution of the Borborema Province have been the subject of continuous debate (e.g., [42,50]). Some authors propose an accretionary model involving terrane accretion episodes throughout the Neoproterozoic [66–70]. In contrast, Neves [50,71] proposed an intracontinental model with the closure of small basins with limited oceanic crust, in agreement with proposals of a contiguous basement beneath the proposed terranes since the Paleoproterozoic [72–75]. Alternatively, a model consisting of a complete Wilson cycle with continental rifting, followed by subduction of large oceanic realms and a subsequent collision has also been proposed [42,52,56,64]. Diverging interpretations regarding the tectonic setting and evolution of the Tonian tectonothermal event (c. 1.0 Ga, Cariris Velhos Event), and a lack of agreement regarding the interpretation and significance of potential Neoproterozoic suture zones and magmatic arcs, make it difficult to achieve a consensus regarding the tectonic evolution of the BP and are beyond the scope of this review.

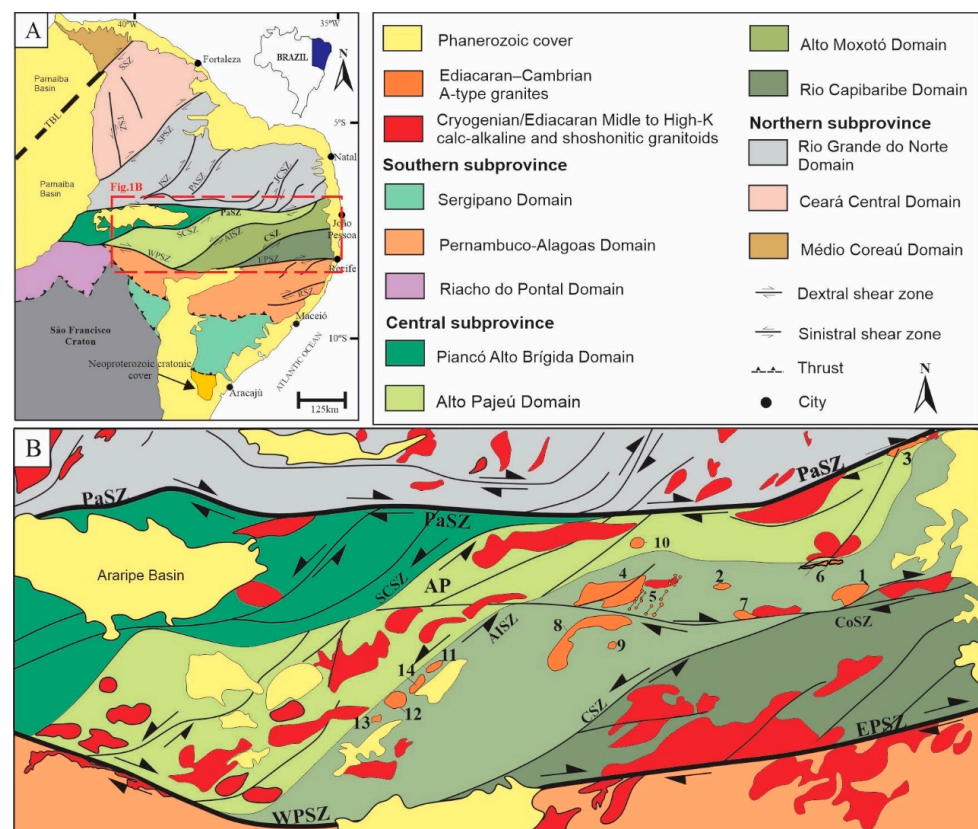


Figure 1. Geological maps illustrating the regional context and the location of the studied plutons [73]. (A) Major domains and shear zones of the Borborema Province [73]. Abbreviations—PaSZ: Patos Shear Zone; WPSZ and EPSZ: West and East Pernambuco Shear Zones; SSZ: Sobral Shear Zone; SPSZ: Senador Pompeu Shear Zone; JSZ: Jaguaribe Shear Zone; JCSZ: João Câmara Shear Zone; PASZ: Portoalegre Shear Zone; RSZ: Riachão Shear Zone; TSZ: Tauá Shear Zone; (B) Central Subprovince of the Borborema Province with studied plutons highlighted in orange (adapted from Lima et al. [73]). Abbreviations—CoSZ: Coxixola Shear Zone; CSZ: Congo Shear Zone; AISZ: Afogados da Ingazeira Shear Zone; SCSZ: Serra do Caboclo Shear Zone. Studied plutons: 1—Aroeiras Pluton; 2—Bravo Pluton; 3—Pilõesinhos Pluton; 4—Serra Branca Pluton; 5—Serra Branca dike swarms; 6—Queimadas Pluton; 7—Marinho Pluton; 8—Prata Complex; 9—Serra da Engabelada Pluton; 10—Serrote Santo Antonio Pluton; 11—Pereiro Pluton; 12—Serra do Velho Zuza Pluton; 13—Açude do Caroá Pluton; 14—Boqueirão Pluton.

During the post-collisional stages, the evolution of the BP was primarily controlled by strike-slip tectonics, with a network of fault zones that favored the formation of local extensional zones. During this period, the BP was affected by the widespread intrusion of high-K post-collisional, 'A-type' plutons and dike swarms, mineralizing events associated with pegmatites, and the influx of hydrothermal fluids during shear zone reactivation, as well as the development of sag basins with the collapse of orogenic chains and rupture of the continental crust [35,40,76–78]. The different groups of A-type granites that intruded the Central Subprovince at c. 580–525 Ma, mark episodes of tectonic shift and provide insights into the post-collisional evolution of the Borborema Province and are the subject of this review [35,37,73].

3. Geological Context of the Studied A-Type Granites

3.1. Introduction

The studied granitoids are primarily intruded within the Alto Moxotó Domain, often near the boundaries with the Alto Pajeú and Rio Capibaribe Domains, whereas the Serrote Santo Antonio and Pilôezinhos plutons are intruded in the Alto Pajeú domain (Figure 1B). The Alto Moxotó Domain comprises Paleoproterozoic units enclosing some Archean nuclei, overlain by Neoproterozoic supracrustal rocks [47,75,79]. The A-type granitic intrusions are associated with E-trending (Aroeiras, Queimadas, Serra Branca, and Marinho e Pilôezinhos) and NE-trending (Boqueirão, Pereiro, Açude do Caroá, Serra do Velho Zuza, Bravo, and Prata Complex) strike-slip shear zones. The Serra da Engabelada intrusion forms an isolated pluton proximal to the Prata Complex (Figure 1B).

3.2. Aroeiras Complex

The Aroeiras Complex intrudes Paleoproterozoic orthogneisses and migmatites, and Cryogenian–Ediacaran metasedimentary rocks and older granitic plutons (Figure 1B). It comprises a 100 km² sigmoidal-shaped igneous complex that was emplaced during the development of an extensional site associated with the synchronous activity of the E-trending dextral Timbauba-Coxixola and NE-trending sinistral Batista shear zones. It comprises felsic sheets dated at 585 ± 6 Ma (U-Pb zircon LA-ICPMS) and small intermediate bodies cut by late felsic dikes dated at 545 ± 4 Ma [35] (U-Pb zircon SHIRIMP).

The Aroeiras Complex comprises porphyritic to equigranular biotite–hornblende monzogranite to biotite syenogranite (Figure 2A), with prismatic allanite and zircon, acicular apatite, and ilmenite mantled by titanite as the main accessory phases. Intermediate lithotypes comprise hornblende–biotite diorite and quartz diorite. Ovoid microgranular mafic enclaves with crenulated borders, double-enclave relations, and hybrid rocks with a rapakivi-like texture are interpreted as evidence for mingling (Figure 2B,C) and mixing processes in the complex [35].

3.3. Bravo Pluton

The Bravo Pluton is a ~40 km² intrusion emplaced at 581 ± 2 Ma (U-Pb zircon LA-ICPMS) between the NE-trending sinistral Cabaceiras and E-trending dextral São José dos Cordeiro shear zones [39]. It comprises leucocratic, coarse-grained to porphyritic biotite syenogranite to monzogranite, with K-feldspar phenocrysts surrounded by a medium-grained matrix composed of quartz, feldspars, and mafic minerals (biotite and amphibole), with titanite, apatite, allanite, Fe-Ti oxides, and zircon as the main accessory phases [39]. Oval-shaped microgranular enclaves with a granodiorite to diorite composition and typical features of hybridization are commonly found along the margin of the pluton. Fine-grained monzogranitic rocks and aplite dikes locally cut the coarse-grained lithotypes.

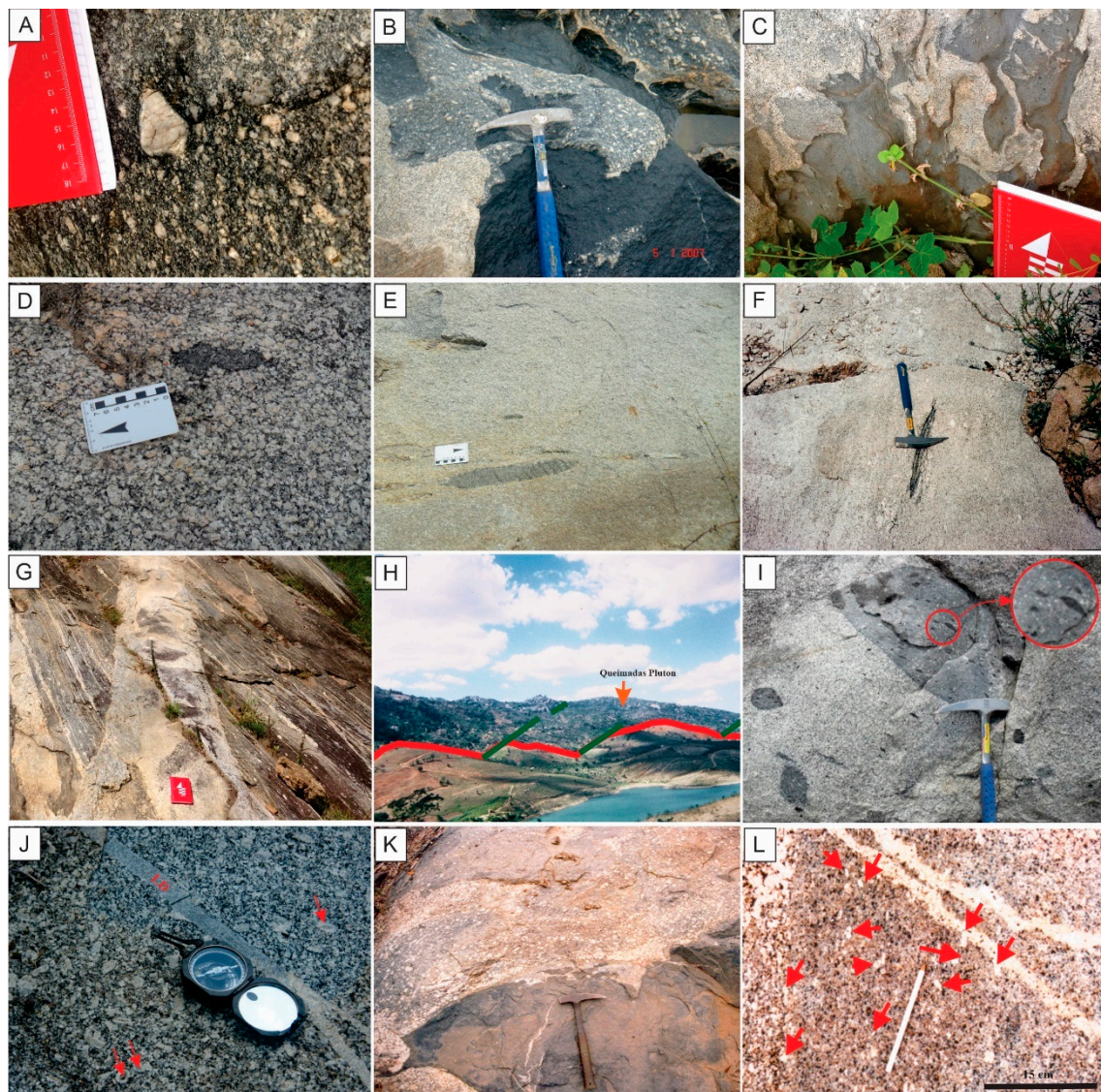


Figure 2. Field aspects of the studied granitoids. (A) Porphyritic syenogranite from the principal facies of the Aroeiras Complex; (B,C) the mingling of diorite with the syenogranite in the Aroeiras Complex; (D) the porphyritic syenogranite of the Pilõezinhos Pluton enclosing the dioritic enclave; (E) a general view of the other facies of the Pilõezinhos Pluton, characterized by fine-grained granitic rocks enclosing an intermediate-composition enclave; (F) typical leucocratic granitic rock from the Serra Branca Pluton; (G) a leucocratic dike from the Serra Branca Suite; (H) the mega-dike field aspects of the Queimadas Pluton. (Red line—contact zone with the basement orthogneiss/migmatite; green line—shear zone; (I) Diorite as enclaves enclosed by felsic granite of the Marinho Pluton. The felsic granite also encloses pockets of mesocratic granite, interpreted as a hybrid rock, which in turn encloses elongated oriented enclaves of mafic diorite (red circles); (J) the dike of rapakivi granite (Marinho Pluton), cut by narrow dikes (up to 20 cm wide) of leucogranite (LD). Red arrows—K-feldspar surrounded by plagioclase of oligoclase composition; (K) the typical features of magmatic interaction between mafic and felsic magma of the Prata Complex; (L) porphyritic granite of the Pereiro Pluton, cut by veins of leucogranites. K-feldspar (red arrows) occurs as euhedral crystals oriented by magmatic flux processes.

3.4. Pilõezinhos Pluton

The c. 566 ± 3 Ma (U-Pb zircon LA-ICPMS) Pilõezinhos Pluton comprises an ENE-elongated intrusion of c. 100 km², located south of the Remígio-Pocinhos shear zone along the boundary between the Northern and Central subprovinces of the Borborema

Province [38]. The Pilõezinhos granitoids consist of equigranular to porphyritic, fine- to coarse-grained syenogranite to monzogranite (Figure 2D,E), intruded into the late Neoproterozoic metasedimentary rocks and Tonian orthogneisses of the Alto Pajeú Domain, in extensional sites created by the synchronous movement of the E-trending dextral Remígio-Pocinhos shear zone (ZCRP) and the NE-trending sinistral Matinhas shear zone, which allowed for the accommodation of the granitic magmas [38].

These granitoids contain quartz as anhedral crystals, recrystallized or subgrain aggregates, microcline phenocrysts, and subhedral and often zoned plagioclase crystals. The main mafic phases are large biotite lamellae and amphiboles. The accessory minerals comprise titanite as the primary crystals or forming coronas around opaque minerals, zoned allanite, and opaque minerals, mainly euhedral ilmenite.

3.5. Serra Branca Suite

The Serra Branca Suite consists of a primary body of ~300 km² (Serra Branca Pluton) and a swarm of granitic dikes (Serra Branca-Coxixola dike swarm) intruded into Paleoproterozoic to Archean gneiss migmatites [35,80]. These granitic intrusions are located north of the E-trending dextral Timbauba-Coxixola Shear Zone and west of the NE-trending sinistral Cabaceiras Shear Zone. U-Pb dating of the Serra Branca Pluton gave a 560 ± 5 Ma crystallization age (U-Pb zircon SHRIMP) [80].

The Serra Branca Pluton comprises small intrusive bodies and sheets of leucocratic, equigranular, medium- to fine-grained biotite syenogranites to monzogranites (Figure 2F), locally containing the xenoliths of surrounding rocks and biotite clots. Quartz, alkali feldspar (perthitic orthoclase and microcline), and plagioclase constitute the mineral framework of these granitoids, along with biotite, the predominant mafic mineral. Apatite, allanite, and zircon are accessory minerals, forming the euhedral to subhedral crystals included within the main mineral phases. Ilmenite is the main Fe-Ti oxide present in these granitoids. The magmatic fabric developed parallel to the NE-trending shear zone foliation is interpreted as evidence that the Serra Branca Pluton is a syn-tectonic intrusion [80]. Magmatic layering with cross-bedding-like features has also been reported in the pluton.

The Serra Branca dikes (Figure 2G) intruded primarily as a NE-trending felsic dike swarm cross-cutting the earlier flat-lying foliation of the basement rocks and the Neoproterozoic metamorphosed supracrustal rocks [35]. Near the Timbauba-Coxixola Shear Zone, the dikes intrude parallel to the steeply dipping mylonitic foliation but show only incipient deformation. The dike swarm comprises porphyritic hornblende-biotite granite to equigranular biotite granite. A Concordia age of 545 ± 3 Ma is interpreted as the crystallization age of these dikes [35].

3.6. Queimadas Pluton

The Queimadas Pluton forms a ~50 km² intrusion dated at c. 550 ± 6 Ma (U-Pb Zircon SHRIMP). It intrudes basement gneisses and migmatites parallel to the E-trending foliation associated with the Campina Grande shear zone (Figure 2H), near the boundary between the Alto Pajeú and Alto Moxotó domains [35,36]. A NE-trending dextral shear zone disrupts the pluton into a mega-boudin-like shape.

The pluton comprises biotite ± amphibole porphyritic monzogranites and granodiorites as the main lithotypes, typically enclosing microgranular mafic enclaves (MMEs) and cut by late fine-grained leucogranite dikes [36]. Biotite and amphibole make up less than 10% of the mode. Allanite and apatite form the euhedral crystals included in the main ferromagnesian minerals, and zircon forms prismatic euhedral or round crystals. Biotite- and amphibole-hosted subhedral crystals of ilmenite, and rare monazite are accessory phases. Mafic microgranular enclaves (MMEs) range in composition from porphyritic quartz-monzonitic to quartz-monzodioritic and are mainly located close to the contact with basement rocks. The Queimadas granitoids show S-C dextral foliation, with the C-foliation plan aligned with the E-trending branch of the Campina Grande dextral shear zone. Biotite

kinks, sigmoidal plagioclase porphyroclasts, quartz ribbons, mosaic texture, boudins, and necking indicate that the pluton was deformed under brittle–ductile conditions [36].

3.7. *Marinho Pluton*

The Marinho Pluton is an ENE-trending elongated intrusion of ~18 km², composed of syenogranites and monzogranites, intruded into Neoproterozoic metasedimentary rocks and Tonian orthogneisses of granodioritic composition. The Marinho Pluton consists of a granitic intrusion, comprising a small stock and associated dikes, intruded in an extensional site, related to the synchronous activity of the dextral E-trending Coxixola shear zone and sinistral NE-trending Carnoio shear zone [81,82].

It comprises two main petrographic facies of a monzogranite to syenogranite composition. The main lithotype, dated at c. 550 ± 3 Ma (U-Pb zircon SHRIMP), is porphyritic and medium-grained and exhibits dioritic enclaves and flow structures [81]. Syn-plutonic dikes and enclaves of a dioritic composition indicate mingling processes. Fine-grained, slightly oriented dikes (~25 m width) of porphyritic rapakivi-like biotite syenogranites dated at c. 527 ± 6 Ma (U-Pb zircon SHRIMP) intrude the main facies of the Marinho Pluton and are cut by fine-grained leucocratic syenogranites (Figure 2I,J) [82].

Petrographically, these granitoids are characterized by perthitic orthoclase and microcline phenocrysts surrounded by a fine-grained matrix comprising subgrain aggregates or ribbon-shaped quartz, feldspars, amphibole, and biotite. Especially in the biotite syenogranite dikes, microcline crystals surrounded by plagioclase rims particularly highlight the rapakivi-like texture. The main mafic phase is biotite partially altered to chlorite. Amphibole locally forms green prisms with bluish-green rims. Titanite, allanite, apatite, and zircon are the main accessory minerals; titanite and allanite often occur as euhedral inclusions in biotite and amphibole, and apatite as acicular crystals.

3.8. *Prata Complex*

The Prata Complex comprises a boomerang-like pluton separated in two parts by a mafic body, intruded into the Archean–Paleoproterozoic migmatite basement [37]. Holanda et al. [40] divided the Prata Complex into two distinct intrusions: a northern intrusion with a U-Pb crystallization age of c. 534 ± 3 Ma (U-Pb zircon SHIRIMP) (Sumé Pluton) and a southern intrusion with a crystallization age of c. 533 ± 4 Ma (U-Pb zircon SHIRIMP) (Santa Catarina Pluton).

The Sumé Pluton, about 250 km² in size, comprises medium- to coarse-grained hornblende–biotite monzo- to syenogranites, with abundant hybrid rocks resulting from mixing with dioritic magma (Figure 2K). The granitoids contain plagioclase, perthitic microcline locally showing plagioclase mantling, amphiboles, and biotite. Subordinate minerals include allanite rimmed by epidote, titanite, apatite, and zircon. Round to angular, sometimes elongated mafic enclaves are frequent and have a dioritic–quartz dioritic composition.

The Santa Catarina Pluton, covering approximately 170 km², primarily consists of coarse-grained porphyritic biotite syenogranite, which is the dominant lithotype and frequently encloses mafic enclaves. This lithotype is characterized by alkali-feldspar phenocrysts exhibiting rapakivi texture. Weak foliation is observed along the southeastern and southern margins of the pluton. In its southern region, a swarm of N-S-trending rhyolite and diabase dikes has intruded into the surrounding gneisses and migmatites, extending into the pluton itself, where the dikes cut the granitoids. Dioritic enclaves in the central–eastern part of the pluton exhibit crenulated contacts, indicating magma mingling and mixing processes between felsic and mafic magmas. These diorites contain rounded and acicular hypersthene crystals, up to 10 mm long and 0.8 mm wide, which are surrounded by augite and hornblende. Additionally, they feature quartz phenocrysts mantled by hornblende and biotite, acicular apatite, small clusters of hornblende and biotite, and poikilitic K-feldspar, all of which indicate magma mixing processes. Allanite is the most

abundant accessory mineral in the syenogranites, occurring in modal amounts of up to 5% and reaching lengths of up to 5 mm.

3.9. Serra da Engabelada Pluton

Near the Prata Complex, there is one small granitic pluton (Serra da Engabelada), along with a gabbro stock and swarms of rhyolite to gabbro-norite dikes [37]. The Serra da Engabelada Pluton comprises a rounded intrusion of approximately 50 km², intruded into the Paleoproterozoic migmatized orthogneisses, located east of the Prata Complex. It consists mainly of coarse-grained, equigranular biotite syenogranites with rare mafic enclaves.

3.10. Serrote Santo Antonio Pluton

The Serrote Santo Antônio Pluton is a 75 km² igneous intrusion, primarily composed of leucocratic, medium- to coarse-grained biotite syenogranite. This pluton is located to the north of the Serra Branca Pluton and is one of the few A-type plutons discussed in this study that is emplaced within the Alto Pajeú Domain, where it intrudes Early Neoproterozoic metamorphosed supracrustal rocks.

3.11. Serra do Pereiro, Serra do Velho Zuza, Açude do Caroá, and Boqueirão Plutons

These plutons were emplaced along the NE-SW sinistral Afogados da Ingazeira Shear Zone, which makes contact between the Alto Pajeú and Alto Moxotó domains of the Central Subprovince in the Borborema Province [83].

The Serra do Velho Zuza (538 ± 23 Ma; U-Pb zircon TIMS), Serra do Pereiro (543 ± 7 Ma; U-Pb zircon TIMS), Açude do Caroá, and Boqueirão plutons show roughly rounded shapes, with the Pereiro and Boqueirão plutons being more elongated, with their major axes parallel to the Afogados da Ingazeira Shear Zone [58]. These plutons are intruded into orthogneisses of the basement and Neoproterozoic supracrustal rocks of the Sertânia and São Caetano complexes [84]. The Serra do Velho Zuza and Boqueirão plutons mainly comprise gray, medium to coarse-grained porphyritic hornblende–biotite monzogranite to syenogranite, while the Serra do Pereiro Pluton comprises hornblende–biotite monzogranite to quartz syenite (Figure 2L). They are composed of K-feldspar phenocrysts in an interstitial matrix composed of quartz, plagioclase, and K-feldspar. Yellow to dark brown biotite and amphibole are the main mafic mineral phases. Epidote, titanite, and opaque minerals are accessory phases.

All plutons contain a small volume of microgranular mafic enclaves. The MMEs are fine-grained and range from diorite to granodiorite. In the Pereiro Pluton, elongated mafic enclaves parallel to the oriented K-feldspar tabular megacrysts define a magmatic fabric.

The Açude do Caroá Pluton stands out from the others by being composed of more mafic rocks, sharing macroscopic and microscopic characteristics with the enclaves found in the other plutons. It comprises mesocratic, fine- to medium-grained biotite quartz-diorite, quartz monzodiorite, and granodiorite, and often contains amphibole- and biotite-rich clots.

4. Whole-Rock Geochemistry

To highlight the chemical characteristics of the studied granitoids, we compiled whole-rock chemical data available in the scientific literature (Aroerias Pluton [35]; Bravo Pluton [39]; Piloezinhos Pluton [38]; Serra Branca Suite [35,80]; Queimadas Pluton [36]; Prata Complex, Serra da Engabelada Pluton, and Serrote Santo Antônio Pluton [37]. In addition, we included unpublished data (Marinho Pluton) and data obtained from a doctoral thesis (Pereiro, Velho Zuza, Açude do Caroá, and Boqueirão plutons [84]). All data are shown in Supplementary Table SI.

The studied granitoids exhibit a wide range of silica contents, with the less evolved rocks (MME and the Açude do Caroá Pluton) showing SiO₂ ranging from 51.3 to 64.8 wt%, while the more acidic granitoids, which are predominant among the studied rocks, have SiO₂ up to 75 wt%. According to the geochemical classification by Frost et al. [19], these granitoids are metaluminous to slightly peraluminous (Figure 3A), with Alumina Saturation Index (ASI)

values ranging from 0.78 to 1.17, and essentially belong to the ferroan series (Figure 3B), with Fe# ($\text{FeO}_t/\text{FeO}_t + \text{MgO}$) values ranging from 0.78 to 0.98, which are commonly associated with magmas that evolved under reducing conditions (ilmenite-series granites [85]). Only five samples show discrepant Fe# values (0.59–0.78); these correspond to samples from enclaves within the Pilôezinhos and Serra Branca plutons, as well as the less evolved facies of the Prata Complex. The granitoids show high total alkali ($\text{K}_2\text{O} + \text{Na}_2\text{O}$) contents (6–10 wt%), and $\text{K}_2\text{O}/\text{Na}_2\text{O}$ ratios ranging from 0.7 to 2.4 (typically > 1), with compositions ranging from alkali-calcic to alkalic in the MALI (modified alkali–lime index) versus the SiO_2 diagram (Figure 3C), with only a few plotting in the calc-alkalic field. This set of geochemical characteristics indicates that the studied plutons are A-type granites. They plot primarily within the field of granites originating in post-collisional settings (post-COLG) in the Rb vs. (Y + Nb) diagram [86] and show (Zr + Nb + Ce + Y) values up to 1700, typical of A-type granites [87] (Figure 4). Additionally, the studied granitoids dominantly plot within the A2-type granite field on the diagram of Eby [34] or straddling the A1-A2 boundary (Figure 5), distinguishing them from pure A1-type granites, which are typically associated with mantle plume activity or hotspots. A2-type granites, on the other hand, have a crustal origin and are generally linked to post-collisional settings. This set of geochemical characteristics indicates that the studied plutons are composed of A₂-type granites.

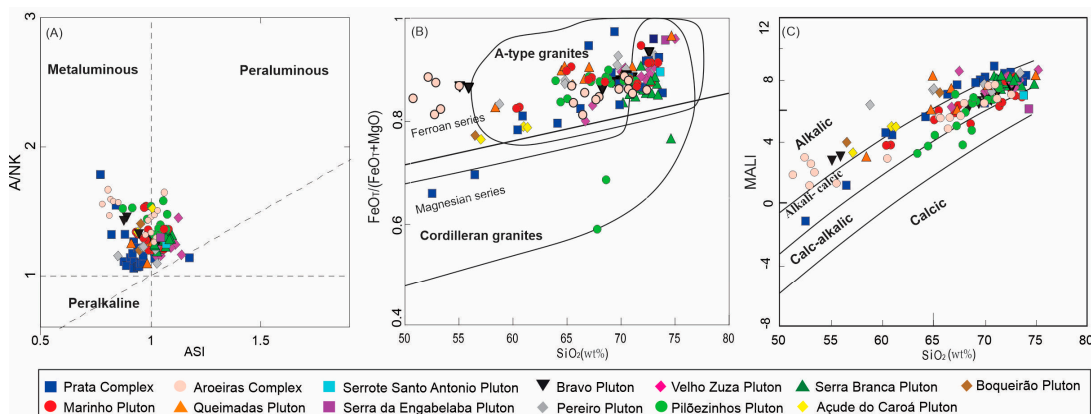


Figure 3. Geochemical characteristics of studied granitoids. (A) Alumina saturation index diagram; (B) $\text{FeO}_T/(\text{FeO}_T + \text{MgO})$ versus SiO_2 diagram; (C) SiO_2 versus Mali (modified alkali lime index) diagram.

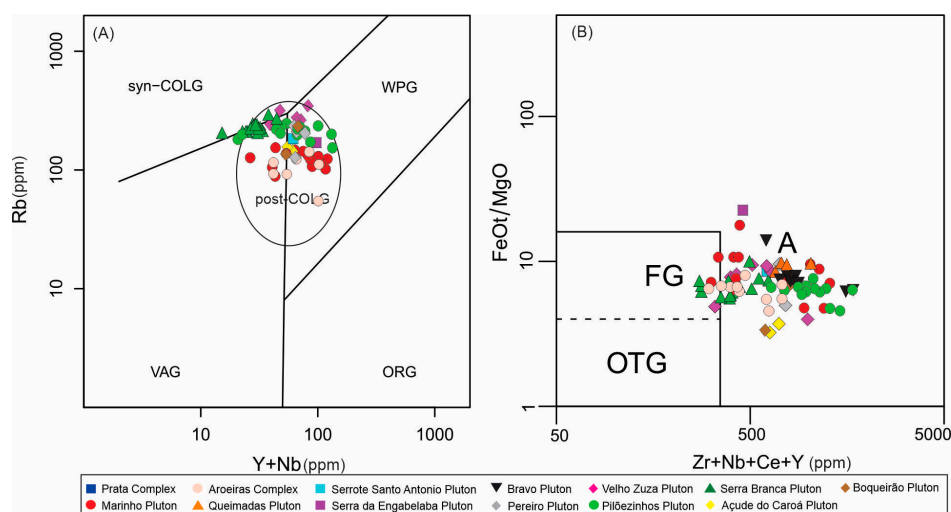


Figure 4. Tectonic setting discrimination diagrams for studied granitoids. (A) Pearce et al. [86]: WPG: within-plate granites; syn-COLG: syn-collisional granites; post-COLG: post-collisional; ORG: ocean ridge granites; VAG: volcanic arc granite; (B) diagram from Whalen et al. [87]: FG: fractionated granite field; OTG: unfractionated granite field; A: A-type granites.

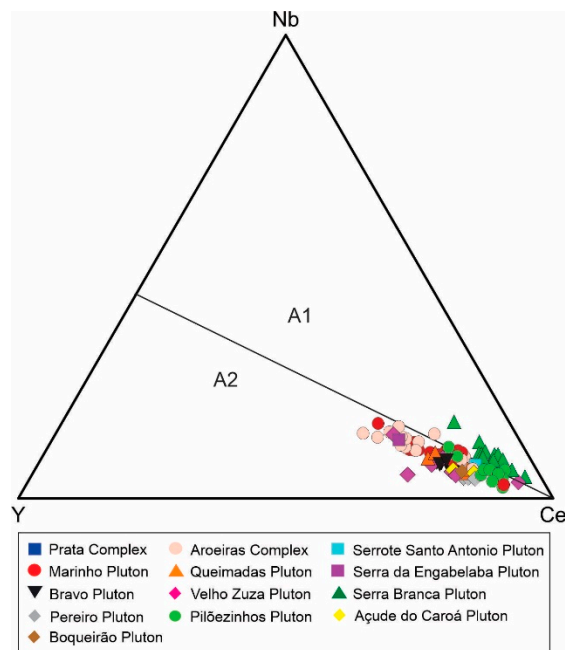


Figure 5. Trace elements of the studied granitoids in the tectonic discriminant diagrams of Eby [34]. A1: Non-orogenic granite; A2: Post-collisional/post-orogenic granite.

5. Mineral Chemistry

The chemical characterization of the mineral phases in the studied granitoids was primarily based on a compilation of data from the scientific literature (Aroeiras Pluton [35]; Bravo Pluton [39]; Pilõezinhos Pluton [88]; Serra Branca Suite [35,89]; Queimadas Pluton [36]; and Prata Complex [37]) and a doctoral thesis (Açude do Caroá, Boqueirão, Velho Zuza, and Pereiro Plutons [84]). Additionally, we included unpublished chemical data for amphibole, biotite, and plagioclase from the Marinho Pluton granitoids, along with new trace element data for zircon from the Queimadas, Marinho, Velho Zuza, and Serrote Santo Antônio plutons. All data are shown in Supplementary Table SII.

5.1. Amphibole

The amphibole structural formulas for the studied samples were calculated based on 23 oxygen atoms and the data are available in the Supplementary Table SII. Amphibole data from the Serra da Engabelaba, Santo Antônio, and Pereiro plutons were absent. Amphiboles were classified using Locock's [90] Excel spreadsheet, which follows the guidelines from the International Mineralogical Association for the Nomenclature of the Amphibole Supergroup [91]. Amphibole analyses show $\text{Na} + \text{K} + \text{Ca}$ values between 1.81 and 3.10 a.p.f.u. and Si^{IV} between 5.95 and 7.10 a.p.f.u. (Figure 6A), which are typically reported in magmatic amphiboles [92]. Ca^{2+} is the dominant constituent in the B site, with concentrations much higher than other ions occupying the B site, displaying ${}^{\text{B}}(\text{Ca} + \Sigma\text{M}^{2+})/{}^{\text{B}}\Sigma$ between 0.85 and 1.00, ${}^{\text{B}}\text{Ca}/\Sigma\text{B} = 0.64\text{--}1.00$ and ${}^{\text{B}}\Sigma\text{M}^{2+}/\Sigma\text{B} = 0.00\text{--}0.21$. The calculated values show that the studied amphiboles have ${}^{\text{B}}(\text{Ca} + \Sigma\text{M}^{2+})/\Sigma\text{B} \geq 0.75$ and ${}^{\text{B}}\text{Ca}/\Sigma\text{B} \geq {}^{\text{B}}\Sigma\text{M}^{2+}/\Sigma\text{B}$, indicating that they belong to the calcium subgroup. The analyses show that in the A site, $\text{A} (\text{Na} + \text{K} + 2\text{Ca})$ values are typically higher than 0.5 and in the C site, $\text{C} (\text{Al} + \text{Fe}^{3+} + 2\text{Ti})$ mostly ranges between 0.5 and 1.5. Therefore, most amphiboles plot in the pargasite–hastingsite field (Figure 6B). In the C site, Fe^{2+} and Fe^{3+} are more abundant than other cations, with the $\text{Fe}\# (\text{Fe}/\text{Fe} + \text{Mg})$ ranging from 0.50 to 0.93, also highlighting the high iron concentrations in these minerals. Additionally, K is typically the most abundant constituent in the A site. Therefore, the studied amphiboles are mostly classified as hastingsite and potassic-hastingsite, although, ferro-pargasite and potassic-ferro-pargasite (Boqueirão, Açude do Caroá, Bravo, Pilõezinhos, Prata, and Queimadas plutons), ferro-hornblende and ferro-ferri-hornblende (Açude do Caroá, Marinho, Prata,

and Queimadas plutons), and potassic-ferro-ferri-sadanagaite (Marinho pluton) are also recognized in the studied samples. It is noteworthy that four analyses each of amphibole from the Prata Complex and Queimadas Pluton, as well as two analyses from the Açude do Caroá diorite, show Mg–hornblende compositions.

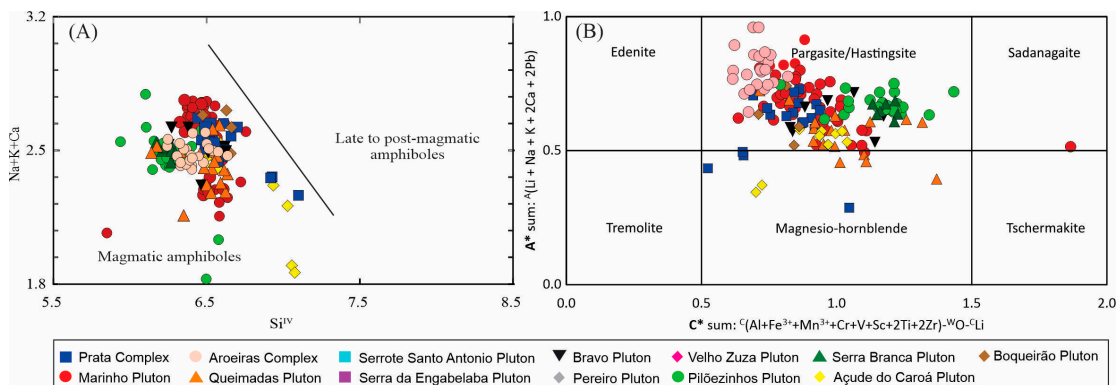


Figure 6. (A) Composition of amphibole crystals plotted in the $Si^{IV} \times (Na + K + Ca)$ diagram [92] indicating a magmatic origin for the studied amphiboles; (B) studied amphiboles in the $A^* \text{ sum: } ^A(Li + Na + K + 2Ca + 2Pb)$ versus $C^* \text{ sum: } ^C(Al + Fe^{3+} + Mn^{3+} + Cr + V + Sc + 2Ti + 2Zr) \cdot ^W O \cdot ^C Li$ calcium amphiboles classification diagram [91], revealing compositions mainly within the pargasite–hastingsite range.

5.2. Biotite

The structural formula was calculated on the basis of 22 oxygen atoms (Supplementary Table SII) and it was assumed that all iron is in the Fe^{2+} state. The compiled analyses of biotite crystals from the studied plutons are consistent with those observed in primary to re-equilibrated primary biotites; no analyses fall in the secondary biotite field (Figure 7A). In the classification diagram by Foster [93], most of the studied biotites are classified as Fe-biotite to siderophyllite. However, five analyses of biotites from the less evolved facies of the Prata Complex show a more magnesian composition (Figure 7B).

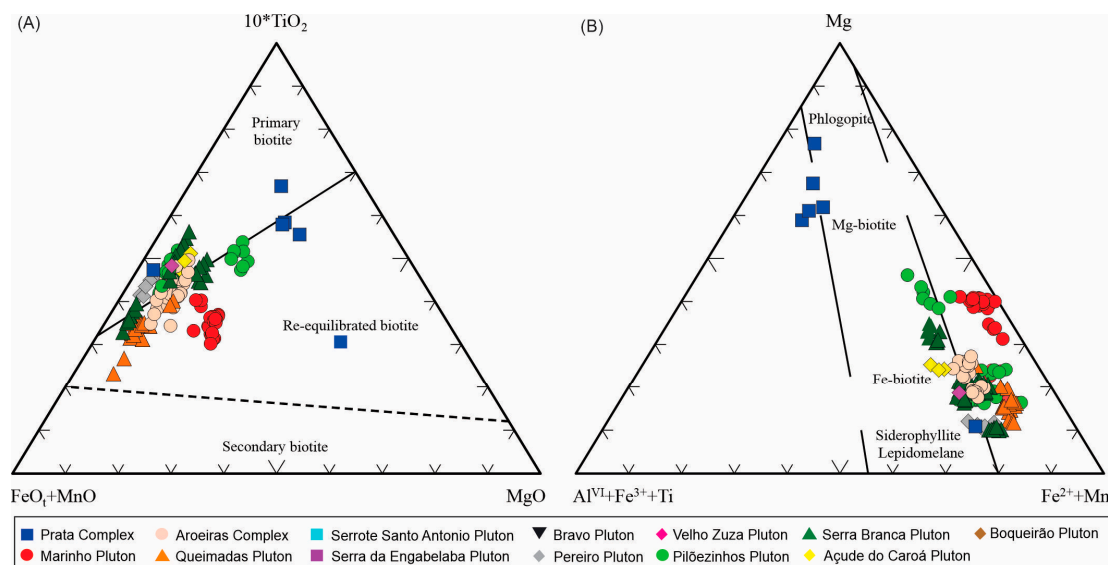


Figure 7. Chemical characteristics of the studied biotite crystals; ternary diagrams produced from Gündüz and Asan [94]. (A) $MgO \times 10TiO_2 \times FeO_t + MnO$ ternary diagram [95], showing the studied biotites straddling between the primary and re-equilibrated fields; (B) Classification of biotite crystals in the $Al^{IV} + Fe^{3+} + Ti \times Fe^{2+} + Mn \times Mg$ ternary diagram [93], showing predominantly Fe-rich compositions.

The Fe# [Fe/(Fe + Mg)] versus SI (solidification index) diagram (Figure 8A) has proven effective in studies involving several plutons, as the chemical trend in biotite is directly linked to the evolutionary character of the host granitoids. The SI is calculated using the formula $[SI = 100 \times MgO / (MgO + FeO + Fe_2O_3 + Na_2O + K_2O)]$, where higher SI values indicate less evolved rocks, while lower SI values indicate more evolved rocks. This correlation between SI values and the degree of evolution in biotite-bearing granites underscores the utility of the SI metric in petrological studies. The biotite crystals of the Prata Complex project at extreme positions on the Fe# versus SI diagram, highlighting the broad compositional spectrum of this intrusion. The biotite analyses from gabbroic rocks yield SI values > 60.0. According to the Speer [95] classification, they are eastonite (Figure 8B). One analysis from a more evolved sample shows SI = 22.50 showing a siderophyllite-rich composition (Figure 8B). The biotites from the Pereiro Pluton yield high Fe# values (0.86–0.88) and low SI (20.78–23.66), consistent with a high degree of magmatic evolution for these host granitoids. The biotites from the Pilõezinhos Pluton have SI values ranging from 28.25 to 53.28. Biotites from dioritic enclaves have SI = 49.03–53.28 and are rich in the eastonite molecule (Figure 8B), whereas the biotites from the more evolved facies have SI from 28.25 to 38.56 and are rich in the siderophyllite molecule. Biotites from all other plutons show siderophyllite-rich compositions (Figure 8B).

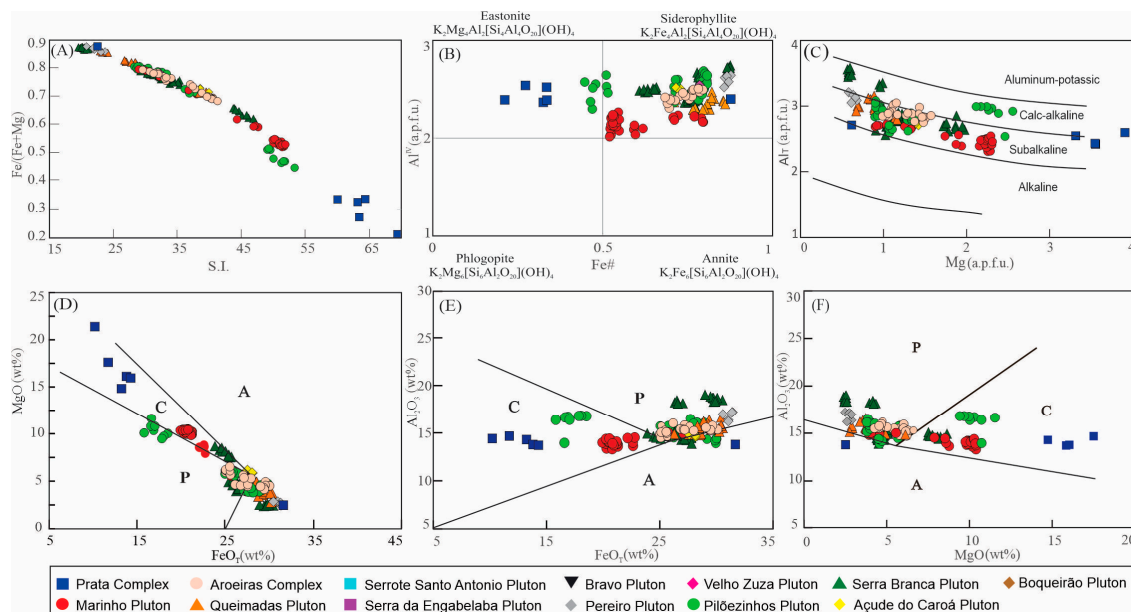


Figure 8. Chemical classification of the studied biotites. (A) Fe/(Fe + Mg) versus S.I. $[100MgO / (MgO + FeO + Fe_2O_3 + Na_2O + K_2O)]$ diagram; (B) Fe# \times Al^{IV} diagram; (C) Mg \times Al_T diagram after Nachit et al. [96]; (D–F) discriminant diagrams after Abdel-Rahman [97]. Legend: A: alkaline anorogenic; C: calc-alkaline; P: peraluminous.

The Al_T contents of the studied biotite crystals range from 2.31 to 3.58 a.p.f.u. In the Nachit et al. [96] classification, the analyses plot in the sub-alkaline series field (Figure 8C), except for a few analyses from the Pilõezinhos Pluton, the Serra Branca Suite and the less evolved lithotypes of the Prata Complex, instead scattering in the calc-alkaline biotite field. In the discriminant diagrams of Abdel Rahman [97] (Figure 8D–F), biotite analyses from the less evolved facies of the Prata Complex, Pilõezinhos Pluton, and a few analyses from the Serra Branca and Marinho plutons, plot into the calc-alkaline series field, whereas biotites from the remaining plutons straddle between the peraluminous and alkaline fields.

5.3. Feldspars

The chemical study of feldspars was conducted using 167 analyses sourced from the literature, along with nine new analyses performed on feldspars from the Marinho

Pluton (Supplementary Table SII). The structural formulae were calculated on the basis of eight oxygen atoms. The plagioclases of the studied granitoids are sodic with albite contents ranging from 41% to 99%. The compositions range mainly from albite to andesine, with two plagioclase analyses from the Prata Complex classified as labradorite (Figure 9). Most of the studied plagioclase crystals exhibit core-to-rim profiles with compositional zoning characterized by an increase in sodium and a decrease in calcium, typical of normal zoning, which is commonly associated with fractionation processes. However, reverse zoning is also observed in some plagioclase crystals from the Prata Complex and the Queimadas Pluton, indicating additional partial melting processes during the magmatic evolution of these plutons or a new influx of more primitive magma into the magma chamber. The Potassic feldspars are mainly orthoclase (Figure 9), with compositions of 58%–98%.

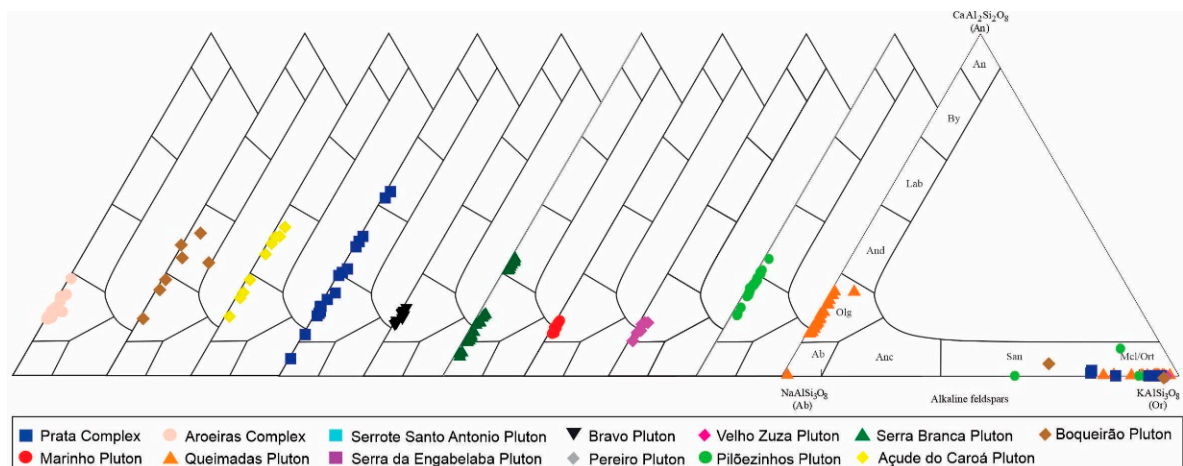


Figure 9. An-Ab-Or ternary diagram for the classification of the studied plagioclase and K-feldspar [98].

5.4. Accessory Minerals

Mineral chemistry data for accessory mineral phases are not available in the literature for all the studied plutons. In the Pilõezinhos Pluton, Lima et al. [88] analyzed opaque minerals which showed a predominance of ilmenite, which is locally surrounded by secondary titanite coronas. The high Al_2O_3 content in secondary titanite ($\text{Al}_2\text{O}_3 > 6\%$; [88]) was interpreted as a distinguishing feature from primary titanite crystals, which exhibit euhedral habit and lower Al_2O_3 content (3.6% to 4.0%).

Santos et al. [89] analyzed apatite crystals from the Serra Branca granitoids and showed structural formulae characterized by contents of Ca at 9.4–9.6, of P at 5.7–5.8, and F at 2.3–2.4, classifying them as fluorapatite [89]. High cerium values also occur in these apatites (1.1%–2.1%).

5.5. Zircon Trace Element Composition

In situ zircon trace element abundances were measured in samples from five plutons (Serrote Santo Antonio, Marinho, Queimadas, Serra do Velho Zuza, and Pereiro) using an Elan 6100DRC ICP-MS instrument coupled to a nanosecond New Wave Research UP-213 laser ablation system, at the Geosciences Center of the São Paulo University. The measurements were undertaken in previously dated zircon grains to avoid inherited grains, using a laser spot of 30 μm , a 4 Hz repetition rate, and an energy fluence of $\sim 10 \text{ J/cm}^2$. The total acquisition time was 120 s, equally divided between background and laser ablation ion signals. The NIST SRM 612 glass wafer was employed as the external calibration standard [99], while an averaged SiO_2 abundance of 31.6% was chosen as the internal standard, following S.R.F. Vlach (pers. communication). The (version 4.0) *Glitter* software [100] was used for drift correction, data reduction, and elemental abundance determinations. Trace element values for the investigated zircon grains are

given in Supplementary Table SIII. Analyses yielding anomalous P, Th, Ti, and LREE were excluded and were interpreted to represent the analysis of microinclusions (e.g., apatite, titanite, or rutile) interfering with the analysis [101–104].

Zircon is an important accessory phase in most granitic samples, except for the highly differentiated ones [105]. Zircon is resistant to alteration and metamorphic processes under a wide range of conditions. Therefore, it is widely used in petrogenetic geochronological studies. Despite its simple chemical composition ($ZrSiO_4$), zircon can accept many minor and trace elements into its crystal lattice, which provides information about the chemical composition of the melt from which the granite crystallized [106–112]. However, concentrations of many nonformula elements, such as LREEs (light rare earth elements), can be modified by hydrothermal and low-temperature fluids [113–115].

Zircon crystals in the studied granites form prismatic euhedral to subhedral grains, ranging from 50 to 250 μm in length and showing {101} pyramid endings, features common to zircons crystallized in granites of the alkaline series [105]. The zircon crystals from the Serrote Santo Antonio granite, however, rarely show pyramidal endings. Cathodoluminescence (CL) images show ubiquitous concentric oscillatory zoning, mainly in the crystal rims. Embayments and narrow overgrowths are recorded mainly in the late dike of the Marinho Pluton (FMJ-55) and the Serra Branca dikes [35], indicating local resorption and reprecipitation potentially associated with hydrothermal processes. Apatite and titanite form microinclusions in zircon from most analyzed samples.

The analyzed zircon grains show high but variable Th/U ratios, reflecting high Th contents. The highest values were recorded in the zircons from the Queimadas granites (0.44–3.36, mean 0.98), whilst the lowest values were recorded in the zircons from the Marinho Pluton (0.24–2.76, mean 0.64). Th/U ratios > 0.2 recorded in zircon grains from all studied plutons are typically associated with magmatic origin [103,116].

Hafnium contents in the studied zircons from all studied plutons range from 7941 to 13,507 ppm (Figure 10). The Y abundances are high in the studied samples, ranging from 465 to 3478 ppm (mean 1568 ppm). Zircons from the Serra do Velho Zuza Pluton yield the highest Y values (956–3478 ppm, mean 1807 ppm). The Nb abundance and Nb/Ta ratios vary widely across all samples. However, the Nb/Ta ratios for most samples are <10, except for the analyses from the Serra do Velho Zuza Pluton, in which Nb/Ta values distinguish two zircon populations: (i) Nb/Ta ratios > 10 due to high Nb abundances (74–228 ppm), and (ii) Nb/Ta ratios < 10 (Figure 10A). Zircon grains from all studied granites show negative correlations between Hf contents and Zr/Hf and Nb/Ta ratios (Figure 10A,B).

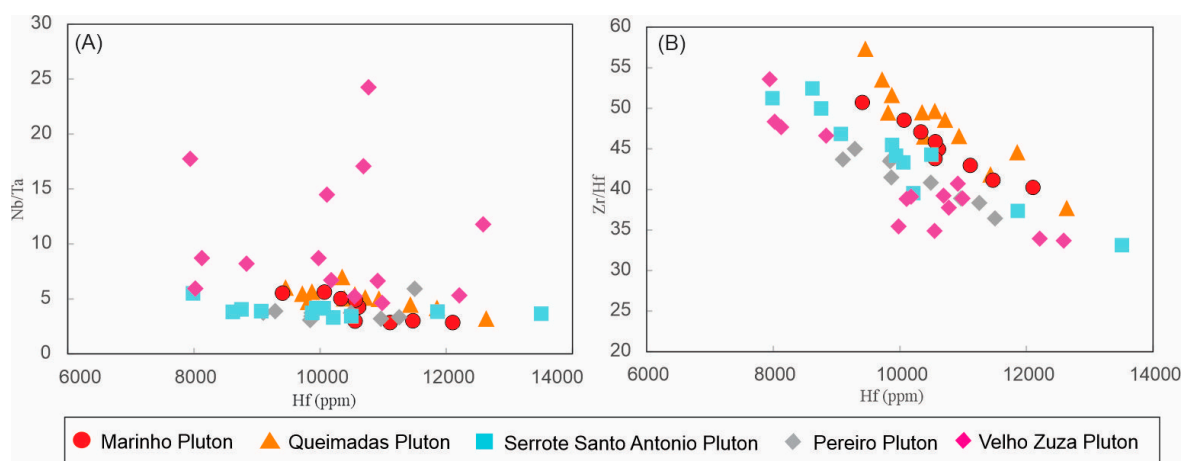


Figure 10. Variation diagrams for studied zircon crystals. (A) Hf (ppm) \times Nb/Ta; (B) Hf (ppm) \times Zr/Hf.

Chondrite-normalized REE patterns (Figure 11A–E) of the zircon grains from all studied granitic plutons are, with some exceptions, similar. The patterns are character-

ized by a steeply rising slope due to HREE enrichment relative to LREEs, positive Ce, and negative Eu anomalies, with Ce/Ce^* [$Ce_N/(La_N \times Pr_N)$] = 1.2–23.6 and Eu/Eu^* [$Eu_N/(Sm_N \times Gd_N)$] = 0.02–0.38. These patterns are typical of igneous zircon [104]. Zircon grains from the Pereiro Pluton show lower LREE abundances (24.7–74.8 ppm), deeper Eu ($Eu/Eu^* = 0.04–0.09$), and higher Ce anomalies ($Ce/Ce^* = 1.88–23.58$) than the other studied granites (Figure 11E). Zircon grains from the rapakivi syenogranite of the Marinho Pluton are characterized, in general, by higher LREE abundance (24.6–1136 ppm) resulting in less steep-rising slope patterns (Figure 11B). Most of the analyzed zircon grains from the Marinho granitoids exhibit slightly positive Ce anomalies [$(Ce/Ce^*)_N = 1.20–2.65$], with only one grain displaying a more pronounced Ce anomaly [$(Ce/Ce^*)_N = 7.98$].

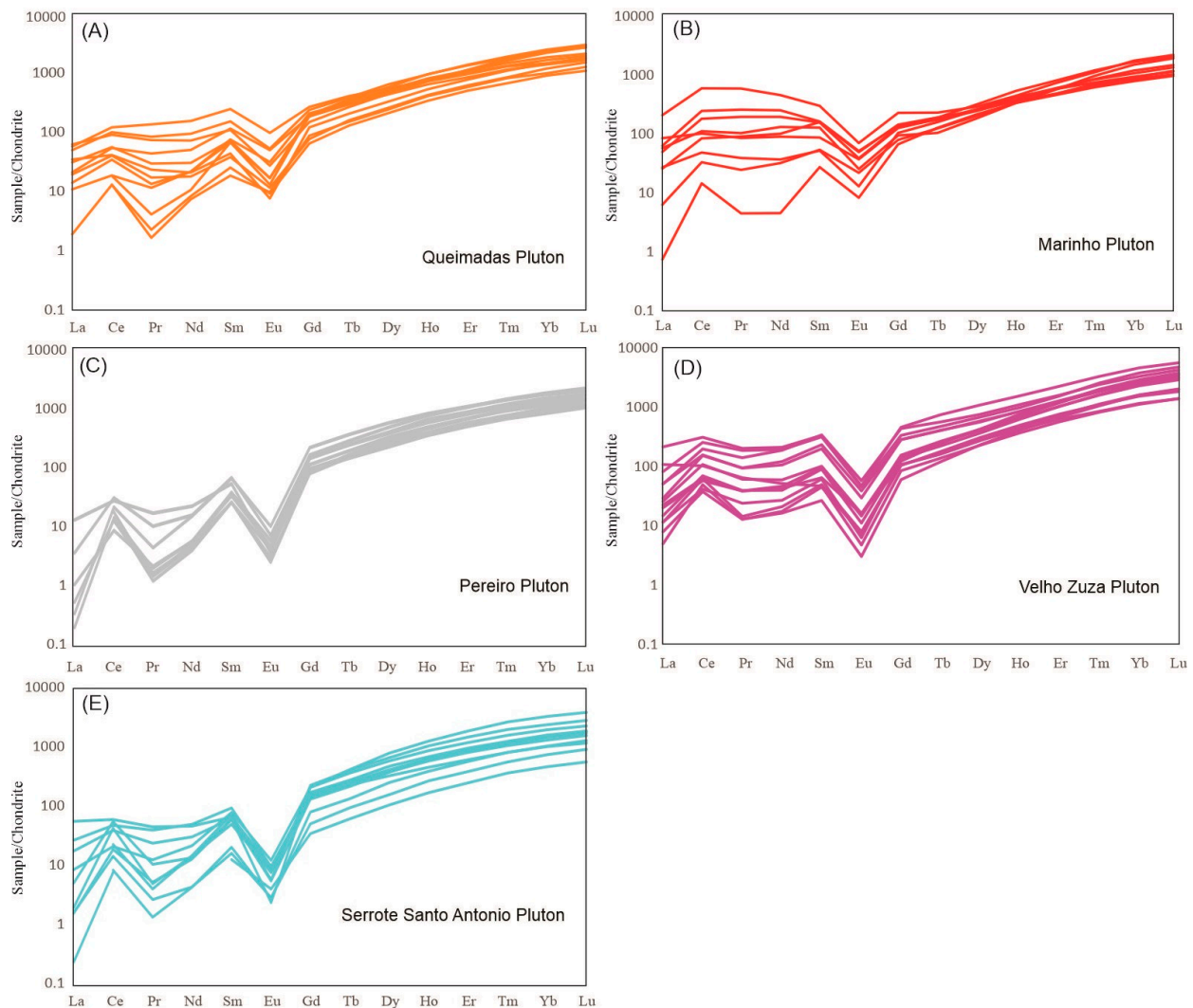


Figure 11. Chondrite-normalized REE patterns [117] of the zircon crystals from the studied plutons. (A) Serrote Santo Antônio Pluton; (B) Marinho Pluton; (C) Queimadas Pluton; (D) Velho Zuza Pluton; (E) Pereiro Pluton.

6. Discussion

6.1. Mineralogical Characterization, Chemical Affinity, and Petrogenetic Implications

Although granites exhibit relatively simple mineralogy, they are notably recognized for their significant modal and chemical variability, which reflects the diverse modes of occurrence and genesis [18]. The mineral composition of granite is a crucial factor in distinguishing the chemical signature and source of the parental magma, offering essential insights into the magmatic evolution processes.

In the studied granitoids, the mafic mineralogy is characterized by Fe-rich calcium amphibole [91] and biotite of siderophyllite composition, which, together with quartz and perthitic feldspars, form the essential minerals. Titanite, allanite, apatite, zircon, and Fe-Ti oxides, predominantly ilmenite, are the most frequently observed accessory minerals. The composition of the mafic minerals, associated with the presence of primary ilmenite crystals, is typical of ilmenite series granites [85], supporting their classification as ferroan A-type granites [23,28]. The analyzed zircons yield high Y, Th, and U consistent with values reported for zircons from A-type granites [118].

According to Xie et al. [119], zircons from aluminous A-type granites exhibit ThO₂ contents of less than 1 wt%, unlike zircons from peralkaline A-type granites, which can reach up to 10 wt%. In the latter, microinclusions of thorite are common due to thorium concentrations exceeding the solubility limit of Th in the zircon structure. However, late alteration of zircon can occur via fluids accumulated at the end of the magmatic evolution of an A-type granite. Most of the zircon grains analyzed from the Queimadas, Marinho, Pereiro, and Serrote Santo Antônio plutons exhibit Th concentrations below 300 ppm. In contrast, in the Velho Zuza Pluton, which is the most aluminous granite (Figure 3A), only one zircon grain shows a Th contents below 300 ppm, while the other analyzed grains display Th concentrations ranging from 335 to 1025 ppm. Santos [120] reported a wide Th variation (60–1250 ppm) in zircon grains from the aluminous A-type Serra Branca granites. Thus, zircon Th contents do not discriminate aluminous A-type from normal A-type granites.

In general, the majority of analyzed zircon grains present high levels of Th and LREEs, in addition, Figure 12 shows positive correlation of LREEs with Th and Y in zircon from of the most plutons. The data presented show that, at least for the studied A-type granites, Th abundance in zircon is not a simple function of the granite composition. It appears to depend on the Th content in the source of the magma, the time of zircon crystallization and the composition of the late hydrothermal fluids. Early crystallized inclusions of allanite and monazite may also influence the available thorium content in the magma. However, microinclusions of these minerals were not detected during the zircon grain analyses, and no other features suggesting the crystallization of thorium-rich early mineral phases were identified.

The chemical composition of biotite can be a valuable indicator of the chemical affinity of the magma from which it crystallized [96,97]. In the studied granites, the biotites chemical compositions reflect an intermediate chemical affinity between peraluminous and alkaline (Figure 8D–F). However, in the discriminant diagram by Nachit et al. [96], the biotite compositions indicate a subalkaline chemical signature (Figure 8C), consistent with the whole-rock chemical compositions of alkali-calcic granitoids (Figure 3C) as well as most A-type granitoids worldwide. The biotites from the more magnesian facies plot within the field of biotites from calc-alkaline granitoids, with some biotites from the Prata Complex showing compositions similar to high Mg-Ti biotites (phlogopite). The granitoids of the Prata Complex exhibit many field features suggestive of interaction with more mafic magmas. Both chemical and field data indicate that mafic melts derived from the lithospheric mantle contributed to the formation of the Prata Complex magma.

The zircon trace element signatures of the studied granites closely align with the findings from the biotite chemical compositions and the whole-rock chemistry. According to Vilalva et al. [121], zircons from rocks of the alkaline association yield Hf < 10,000 ppm, whereas zircons from rocks of the subalkaline rock association yield Hf > 10,000 ppm. However, this limit cannot be applied to classify the studied rocks, because values both above and below this threshold have been shown in the same sample. On the other hand, it could suggest granite compositions in the transition between subalkaline and alkaline associations.

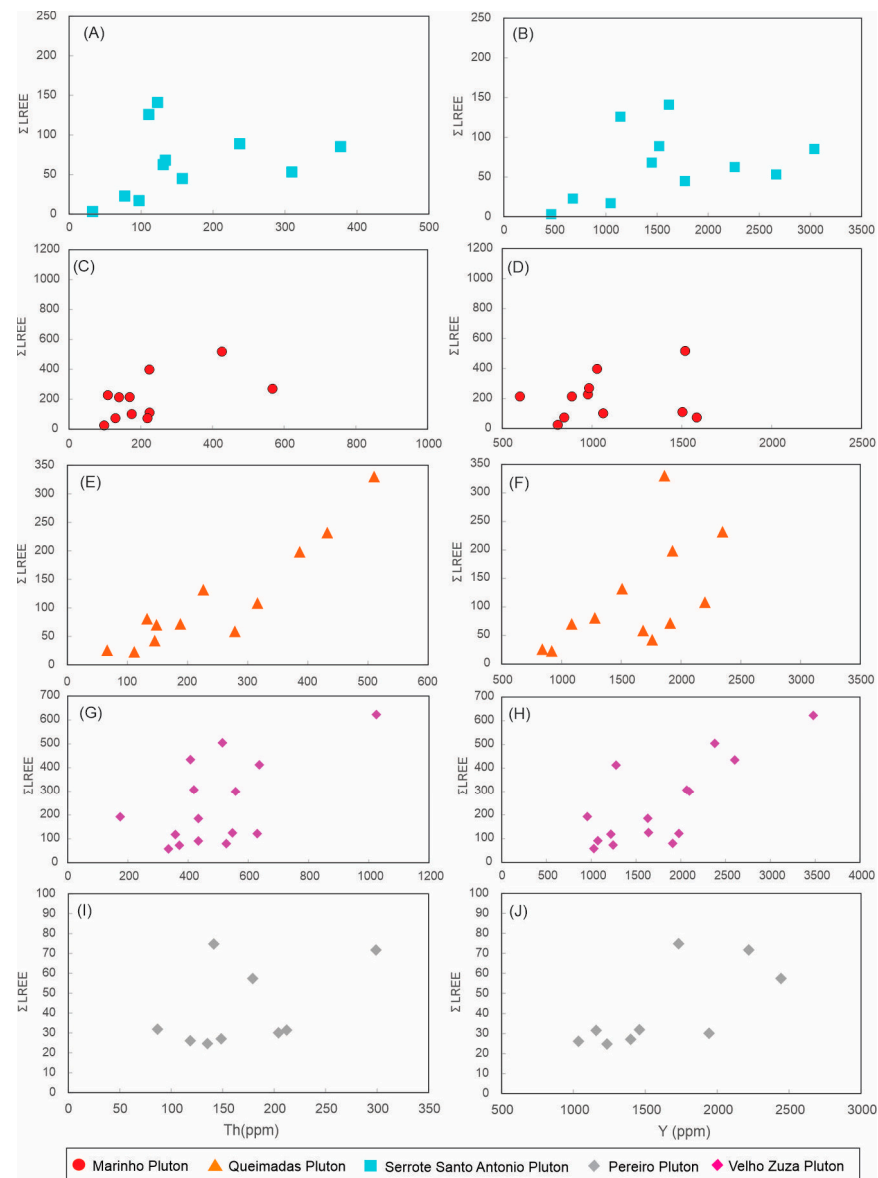


Figure 12. Th \times Σ LREE and Y \times Σ LREE plot for studied zircon crystals. (A,B) Serrote Santo Antônio Pluton; (C,D) Marinho Pluton; (E,F) Queimadas Pluton; (G,H) Velho Zuza Pluton; (I,J) Pereiro Pluton. A zircon grain from the Marinho Pluton (FMJ-55-Zr-12) has anomalous Th and LREE concentrations (Supplementary Table SIII) and, therefore, was not included in (C,D).

Breiter et al. [118] used zircon trace elements from an extensive dataset to discriminate zircon from highly evolved, evolved, and normal A-type and S-type granites. They found that zircon Zr/Hf ratios < 25 are typical of strongly evolved granites, Zr/Hf ratios in the 25–55 intervals characterize evolved granites, while normal granites have Zr/Hf ratios > 55 . Except for one grain of the Queimadas Pluton, zircon grains from all studied plutons exhibit Zr/Hf ratios between 33 and 54, these being typical for evolved A-type granites, according to Breiter et al. [118]. Hawkesworth and Kemp [8] used zircon Th/U and Nb/Hf ratios to discriminate between I-type and peralkaline A-type granites. The zircon of the studied granites plots within the A-type granitoid field (Figure 13A). The correspondence between the studied zircon grains and the A-type field in the Nb/Hf vs. Th/U plot by Hawkesworth and Kemp [8] suggests that, in addition to distinguishing between zircon from peralkaline A-type granites and I-type granites, this diagram is also effective in discriminating between zircon crystals from I-type granites and non-peralkaline A-type granites.

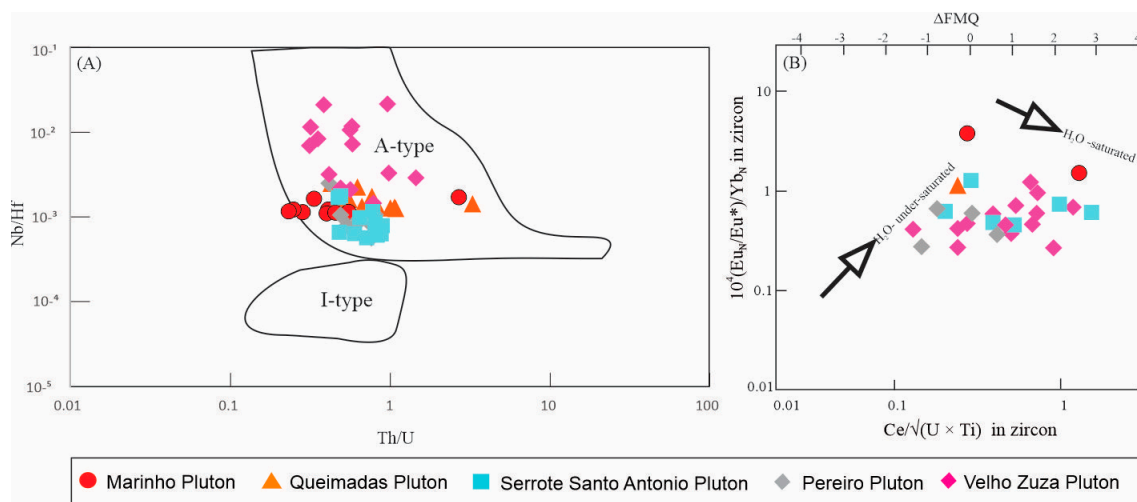


Figure 13. Discriminant diagrams based on the trace element chemistry of the analyzed zircons. (A) An Nb/Hf vs. Th/U plot for the studied zircon crystals. The A-type and I-type fields are from Hawkesworth and Kemp [8] using zircon data of peralkaline A-type granites akin to those of Nigeria and I-type granites from the Lachlan Fold Belt (SE Australia), respectively; (B) the $10^4(\text{Eu}/\text{Eu}^*)_N/\text{Yb}_N$ vs. $\text{Ce}/\sqrt{(\text{U} \times \text{Ti})}$ plot [112] for the studied zircon crystals.

The water content in A-type granites is a frequently debated topic, although it is traditionally accepted that these granitoids evolve from anhydrous to undersaturated magmas. The chemical composition of zircon can provide valuable insights into this issue. According to Loucks et al. [122], during the ascent of a volatile-rich magma, zircon and plagioclase co-precipitate, while hydrothermal fluid is exsolving and segregating from the decompressing melt. These processes produce a negative correlation between zircon $(\text{Eu}/\text{Eu}^*)_N/\text{Yb}_N$ (a useful melt hygrometer) and zircon $\text{Ce}/\sqrt{(\text{U} \times \text{Ti})}$ (a useful indicator of melt oxidation state). Most zircon grains from the Marinho, Queimadas, and Pereiro plutons exhibit Ti concentrations below the detection limit, making it difficult to establish a reliable correlation between $(\text{Eu}/\text{Eu}^*)_N/\text{Yb}_N$ and $\text{Ce}/\sqrt{(\text{U} \times \text{Ti})}$ ratios (Figure 13B). Two grains from the Marinho Pluton show Ti concentrations above the detection limit along with high $(\text{Eu}/\text{Eu}^*)_N/\text{Yb}_N$ values, forming a negative trend in Figure 13B, suggesting that these zircon grains may have crystallized from a more hydrous melt. The four analyses from the Pereiro granitoids and the six analyses from the Serrote Santo Antonio Pluton, which show Ti concentrations above the detection limit, form flat trends. Zircon grains from the Velho Zuza Pluton display a weak positive correlation between $(\text{Eu}/\text{Eu}^*)_N/\text{Yb}_N$ and $\text{Ce}/\sqrt{(\text{U} \times \text{Ti})}$ ratios (Figure 13B), indicating crystallization from an H_2O -undersaturated melt.

6.2. Estimation of Crystallization Parameters

6.2.1. Temperature

In previous studies [39,84,88,89], the crystallization temperatures of the studied A-type magmas were determined using the classic amphibole–plagioclase geothermometer, which is based on the plagioclase–amphibole equilibrium [123]. This geothermometer yielded temperatures (Table 1) ranging from 810 to 730 °C for the Aroeiras Complex, 790 to 740 °C for the Pilõezinhos Pluton, 710 to 560 °C for the Serra Branca Suite, 780 to 580 °C for the Bravo Pluton, and 810 to 780 °C for the Açude do Caroá Pluton.

Amphiboles are complex hydrous silicate minerals that can incorporate many elements into their structure, such as aluminum, iron, magnesium, and titanium. The temperature and pressure conditions strongly influence these compositional variations during crystallization. Based on the concentrations of major oxides in amphiboles, Ridolfi et al. [124] and Ridolfi and Rezzulli [125] developed geothermometers with an associated error of ≥ 50 °C. The amphibole–liquid thermometer proposed by Putirka [126] enhanced the precision of Ridolfi and Rezzulli's [125] geothermometer (± 30 °C). Putirka's thermometer [126] was

applied to the studied granitoids; the lowest temperatures were recorded in the Bravo Pluton (730–650 °C), while the Açude do Caroá Pluton granitoids exhibited temperatures as high as 880 °C, the highest calculated by this geothermometer among the studied plutons.

Zr saturation thermometry was performed to infer the liquidus temperatures of the studied magmatic systems. The solubility of zircon in crustal melts is influenced by both melt composition and temperature [127–129], making the concentration of Zr in whole-rock compositions a valuable tool in thermometric studies of magmatic melts. The temperatures obtained using the calibration proposed by Watson and Harrison [126] for the studied plutons are presented in Table 1. Temperatures range from 790 to 690 °C in the Aroeiras Complex and from 950 to 770 °C in the Pilõesinhos Pluton. For the other granitoids, the temperature values fall within the range covered by these two plutons (950–690 °C).

During the zircon analyses, apatite microinclusions were identified within zircon, suggesting that using the apatite saturation thermometer [130] may be more appropriate for determining the liquidus temperatures of the studied magmatic systems. The temperatures obtained using this geothermometer are shown in Table 1. The less evolved granitoids and those enclosing large number of mafic enclaves, with evidence for magma mixing and mingling yielded the highest temperatures (1160–740 °C). On the other hand, granitoids free of mafic enclaves or containing only rare mafic enclaves (the Velho Zuza, Boqueirão, Serra Branca, Serrote Santo Antonio and Pereiro plutons) exhibit a more restricted and somewhat lower temperature range (1000–780 °C).

The bar graph (Figure 14) illustrates the temperature range at which the studied granitic magmas crystallized. The highest temperatures (liquidus) were obtained using the apatite saturation thermometer [130], while the lowest temperatures correspond to those determined by the amphibole–liquid thermometer of Putirka [126]. Because amphibole data are not available for the Serra do Velho Zuza, Serrote Santo Antônio, Serra da Engabelada, and Pereiro plutons, the minimum crystallization temperatures for these granitoids were inferred from the lowest temperature, provided by zircon saturation thermometer with calibration by Watson and Harrison [129].

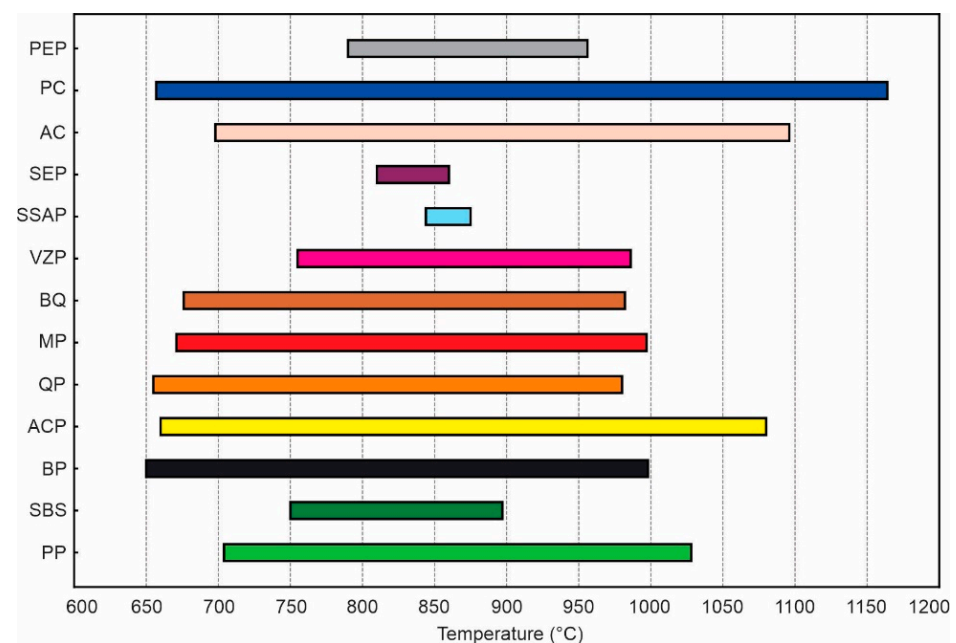


Figure 14. Bar graph illustrating the temperature range at which the studied magmas crystallized. Colors as in the other figures. Abbreviations: PP—Pilõesinhos Pluton; SBS—Serra Branca Suite; BP—Bravo Pluton; ACP—Açude do Caroá Pluton; QP—Queimadas Pluton; MP—Marinho Pluton; BP—Boqueirão Pluton; VZP—Velho Zuza Pluton; SSAP—Serrote Santo Antônio Pluton; SEP—Serra da Engabelada Pluton; AC—Aroeiras Complex; PC—Prata Complex and PEP—Pereiro Pluton.

6.2.2. Pressure

To estimate the pressure in granitic magmatic systems, the total aluminum-in-hornblende barometer is commonly used [131–133]. However, the proposed calculations do not apply to the granitic rocks from this study, as they exhibit higher temperature ranges than those used in the original calibration (655–700 °C). Furthermore, the studied A-type granites have iron-rich amphiboles with $Fe/(Fe + Mg) > 0.65$ associated with low fO_2 conditions which typically result in an increase in Al substitution producing unreliable geobarometer results [132]. New equations for the aluminum-in-hornblende geobarometer have been proposed over the past decades, incorporating increasingly refined natural and experimental data with reduced uncertainties [124,125,134]. However, Putirka [126] highlights that most of these aluminum-in-hornblende geobarometers, including the more recent calibrations, must adhere to the conditions outlined by Anderson and Smith [132]. This requirement makes it difficult to apply geobarometers to rocks that crystallized under low fO_2 , such as A-type granites.

Mutch et al. [134] developed a geobarometer that combines selected experimental data with a wide range of new experimental results. The calibration, performed at near-solidus temperatures and covering a broad pressure range (0.8 to 10 kbar), applies to a wider range of granitic rocks. We applied this geobarometer to determine the crystallization pressures of the studied granitoids (Table 1). Figure 15 illustrates the pressure range for the crystallization of the studied granitic magmas. The lowest pressures were recorded in the granitoids of the Açude do Caroá Pluton (2.5–4.6 kbar), while the Pilôezinhos Pluton granitoids exhibited the highest pressures (5.2–7.0 kbar). The geobarometer developed by Mutch et al. [134] applies to granitoids containing the mineral assemblage amphibole + plagioclase + biotite + alkali feldspar + quartz + ilmenite/titanite + apatite + magnetite. Considering this mineral assemblage is common in the studied granitoids, the obtained pressures are considered reliable. Additionally, the Al^{IV} and Al^{VI} values of the amphiboles analyzed in this study fall within the pressure range obtained through the geobarometer of Mutch et al. [134]. The large pressure variations observed within some individual plutons can be explained by the crystallization of amphibole grains at greater depths, subsequently transported by the magma to shallower levels where the rest of the pluton crystallized.

Table 1. Estimation of temperature and pressure for the studied plutons. Abbreviations: PP—Pilôezinhos Pluton; SBS—Serra Branca Suite; BP—Bravo Pluton; ACP—Açude do Caroá Pluton; QP—Queimadas Pluton; MP—Marinho Pluton; BP—Boqueirão Pluton; VZP—Velho Zuza Pluton; SSAP—Serrote Santo Antônio Pluton; SEP—Serra da Engabelaba Pluton; AC—Aroeiras Complex; PC—Prata Complex and PEP—Pereiro Pluton.

Plutons	PP		SBS		BP		ACP		QP		MP		BQ	
Temperature (°C)	Min	Max	Min	Max	Min	Max	Min	Max	Min	Max	Min	Max	Min	Max
Blund and Holland [123]	745	795	560	711	581	785	776	812	-	-	-	-	-	-
Putirka [126]	704	758	750	789	650	730	660	876	655	736	671	802	676	691
Watson and Harrison [129]	772	946	743	838	847	893	804	826	752	903	795	930	857	857
Harrison and Watson [130]	916	1028	784	897	882	998	1037	1080	757	980	865	997	982	982
Pressure (kbar)	Min	Max	Min	Max	Min	Max	Min	Max	Min	Max	Min	Max	Min	Max
Mutch et al. [134]	5.2	7.0	5.98	6.45	4.53	6.39	2.5	4.6	3.85	6.72	3.94	5.38	4.29	5.21
Plutons	VZP		SSAP		SEP		AC		PC		PEP			
Temperature (°C)	Min	Max	Min	Max	Min	Max	Min	Max	Min	Max	Min	Max		
Blund and Holland [123]	-	-	-	-	-	-	733	809	-	-	-	-		
Putirka [126]	-	-	-	-	-	-	698	740	657	769	-	-		
Watson and Harrison [129]	755	895	844	844	810	810	687	790	804	916	790	878		
Watson and Harrison [130]	790	986	875	875	860	860	804	1096	714	1164	851	956		
Pressure (kbar)	Min	Max	Min	Max	Min	Max	Min	Max	Min	Max	Min	Max		
Mutch et al. [134]	-	-	-	-	-	-	4.01	5.75	-	-	-	-		

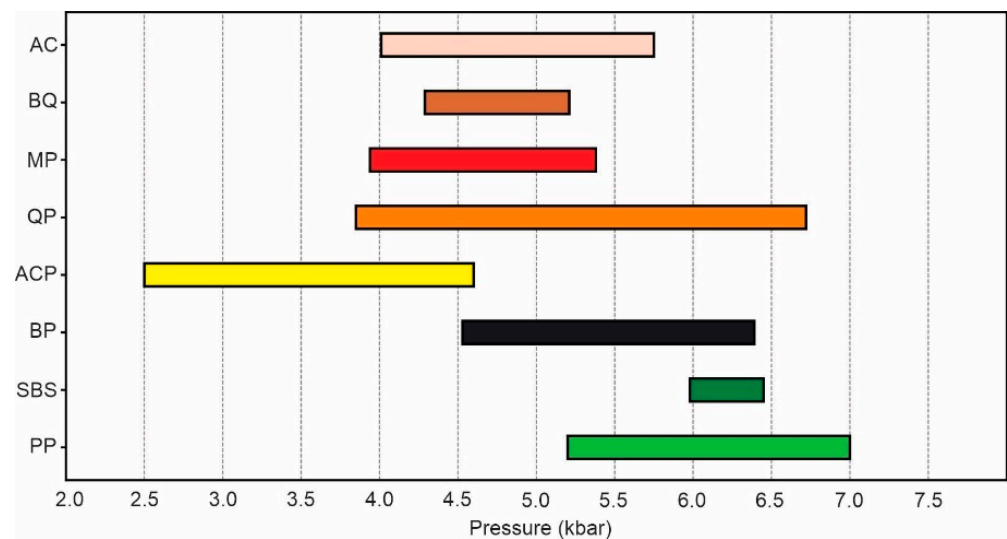


Figure 15. Bar graph illustrating the crystallization pressures of the studied granitoids. PP—Pilõezinhos Pluton; SBS—Serra Branca Suite; BP—Bravo Pluton; ACP—Açude do Caroá Pluton; QP—Queimadas Pluton; MP—Marinho Pluton; BQ—Boqueirão Pluton and AC—Aroeiras Complex.

6.2.3. Oxygen Fugacity

The compositions of biotite, amphibole, and Fe-Ti oxides were also analyzed to estimate the oxygen fugacity (fO_2) of the studied granitoids, as these minerals are highly sensitive to variations of fO_2 . Previous studies have demonstrated that the composition of these phases can be effectively used as proxies for assessing oxygen fugacity in magmatic systems [29,135,136]. The amphiboles in the studied granitoids show a slight variation in Fe# [$Fe/(Fe + Mg)$], with most falling within the range of 0.7 to 0.9. The amphiboles are thus iron-rich, and their Fe# values are characteristic of crystallization under low to intermediate fO_2 conditions (Figure 16A). The $Fe/(Fe + Mg)$ values of the studied biotites follow the same patterns observed in the amphibole compositions (Figure 16B). Most of the studied biotite have $Fe# > 0.65$, similar to those reported by Anderson et al. [137] for biotite of granites that originated from magmas crystallizing under low fO_2 . The composition of the mafic minerals aligns with the overall geochemical signature of these rocks, which predominantly belong to the ferroan series of Frost et al. [19]. This series is typically associated with magmas that evolved under reducing conditions, characteristic of the ilmenite series granites described by Ishihara [85]. It is important to note that some of the analyzed biotites and amphiboles exhibit low Fe# values; these were obtained from Açude do Caroá diorites and the less evolved facies of the Prata Complex, as well as the Pilõezinhos and Marinho plutons. As they are more magnesian, these samples plot in the field associated with minerals crystallized under more oxidizing conditions, or that crystallized from a magma of more basaltic composition (dioritic) and higher temperature, which agree with the conspicuous presence of mafic enclaves. The granitoids of the Pilõezinhos and Serra Branca plutons are the only granitoids among the ones studied, with reported detailed studies of opaque minerals [88,89]. In these granitoids, the Fe-Ti oxides are predominantly primary ilmenite crystals, which agree with the mineral and whole-rock chemistry data reported in the literature. These integrated data suggest that the A-type granites of the Central Subprovince of the Borborema Province crystallized from magmas that evolved under low fO_2 conditions, similar to most A-type granites worldwide.

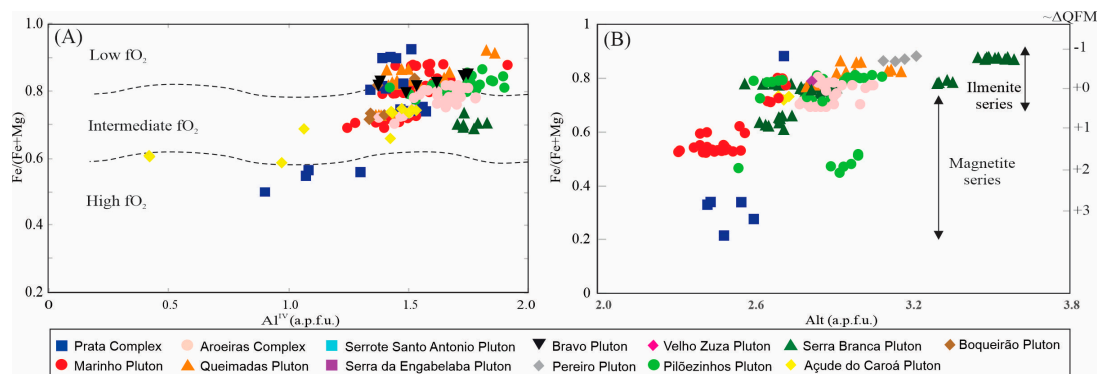


Figure 16. Chemical diagrams for inferring fO_2 conditions. (A) $Al^{IV} \times Fe/(Fe + Mg)$ diagram for the studied amphiboles, with fields according to Anderson and Smith [132]; (B) $Al_T \times Fe/(Fe + Mg)$ diagram for the studied biotites.

6.3. Post-Magmatic Processes

The zircon REE patterns characterized by positive Ce anomalies and negative Eu anomalies and high Th/U ratios recorded in zircon grains from all studied plutons are characteristics of igneous zircon. However, relatively high LREE abundances were recorded in zircon grains from Marinho, Serra do Velho Zuza, and Queimadas plutons (Figures 11 and 12), associated with high Y abundances and a positive correlation between $\Sigma LREE$ and Y, suggesting zircon alteration by LREE- and HFSE-enriched late hydrothermal fluids or the precipitation of zircon from these fluids. The presence of hydrothermal zircon is evident in the projection of the zircon compositions in the $(Sm/La)_N$ versus $(Ce/Ce^*)_N$ bivariate discriminant plot (Figure 17) with magmatic and hydrothermal zircon fields after Hoskin [115]. This bivariate plot shows clearly that the zircon grains from the Pereiro granites and some from the Serrote Santo Antonio granites are the least hydrothermally altered zircon grains, while most of the analyzed zircon grains fall within the hydrothermal zircon field (Figure 17). The presence of zircon grains with both higher- and lower-LREE abundances in the same rock, suggests that the zircon LREE and HFSE enrichment involved both alteration of previously crystallized grains by hydrothermal fluids and zircon crystallization from these fluids. Our data agree with earlier studies showing that hydrothermal alteration of zircon is a common process in evolved to highly evolved A_2 -type granites [118,119,121,138].

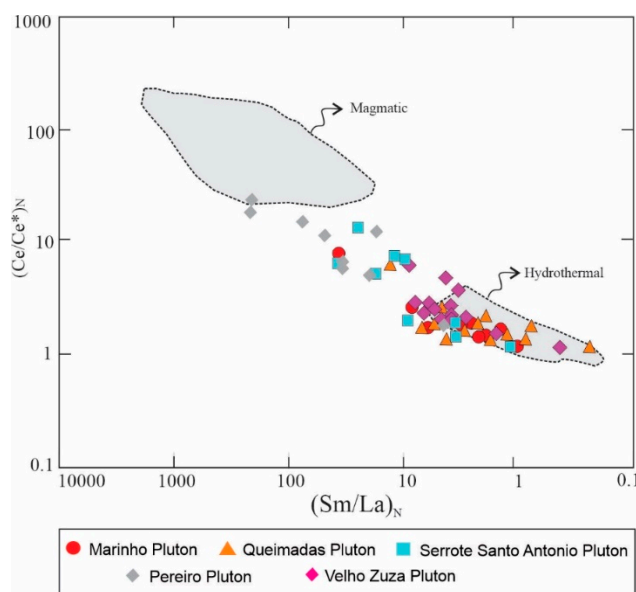


Figure 17. Bivariate discriminant plot $(Sm/La)_N \times (Ce/Ce^*)_N$ of the analyzed zircon crystals.

7. Conclusions

Based on a thorough review of available mineral chemistry and whole-rock geochemistry data from 13 plutons and a dike swarm, including some complementary data, along with new zircon trace element data from five of those plutons, crystallization conditions and post-magmatic processes and their implications for the genesis of Ediacaran–Cambrian A-Type granites from the Central Subprovince of the Borborema Province were evaluated.

These granitoids form small bodies, except for the larger Prata Complex, and were intruded into Paleoproterozoic gneisses and migmatites or Neoproterozoic supracrustals between approximately 580 and 525 Ma, succeeding large intrusions of post-collisional high-K granitoids (590–580 Ma). Several intrusions contain numerous mafic enclaves indicating magma mixing and mingling as an important component in their formation. This is supported by the wide compositional variation in mafic minerals within some of the plutons, revealing that interactions between felsic and mafic magmas played a significant role in the magmatic evolution of those plutons. The mineral assemblages of these granitoids, the chemical composition of the mafic minerals, including siderophyllite-rich biotite and iron-rich calcic amphiboles, the sub-alkaline signature of the biotites, and the zircon trace element composition, align with the whole-rock chemistry. These characteristics classify them as ferroan, alkali-calcic, and dominantly metaluminous granitoids, which are typical features of A-type granites. The crystallization parameters derived from mineral chemistry show temperatures ranging from 1160 to 650 °C in the granitoids containing numerous mafic enclaves, and from 990 to 680 °C in the more evolved granitoids. Crystallization pressures, determined using the Al-in-amphibole geobarometer, mostly range from ~4.0 to 7.0 kbar, corresponding to crustal depths of ~12 to 21 km. The mineral assemblages characterized by Fe-rich mafic phases and ilmenite show that the studied A-type granites crystallized under low fO_2 conditions, akin to classical ferroan A-type granites. We highlight that the zircon trace elements indicate hydrothermal alteration in some of the studied granites, which appears to be a common feature of high-SiO₂ A-type granites. Most of the studied A-type granites intruded within or near shear zones. Thus, the post-magmatic hydrothermal alteration observed in zircon crystals may be associated with the reactivation of these shear zones.

Supplementary Materials: The following supporting information can be downloaded at: <https://www.mdpi.com/article/10.3390/min14101022/s1>. Table SI: Whole-rock geochemistry data; Table SII: Mineral chemistry data; Table SIII: Zircon trace element composition.

Author Contributions: Conceptualization, J.V.d.L. and I.d.P.G.; methodology, J.V.d.L. and I.d.P.G.; software, J.V.A.d.A., C.C.G.B., and L.d.S.; validation, J.V.d.L., I.d.P.G., J.V.A.d.A., and A.F.d.S.F.; formal analysis, I.d.P.G. and J.V.d.L.; investigation, J.V.d.L., I.d.P.G., J.V.A.d.A., and C.C.G.B.; resources, I.d.P.G.; data curation, J.V.d.L. and C.C.G.B.; writing—original draft preparation, J.V.d.L. and I.d.P.G.; writing—review and editing, J.V.d.L., I.d.P.G., J.V.A.d.A., L.d.S., and A.F.d.S.F.; supervision, J.V.d.L. and I.d.P.G.; project administration, I.d.P.G. All authors have read and agreed to the published version of the manuscript.

Funding: This research received no external funding.

Data Availability Statement: The original contributions presented in the study are included in the article/supplementary material, further inquiries can be directed to the corresponding authors.

Acknowledgments: We would like to express our heartfelt gratitude to the three anonymous reviewers for their insightful comments and constructive feedback, which significantly enhanced the quality of our manuscript.

Conflicts of Interest: The authors declare that they have no conflicts of interest.

References

1. Wedepohl, K.H. Chemical Composition and Fractionation of the Continental Crust. *Geol. Rundsch.* **1991**, *80*, 207–223. [[CrossRef](#)]
2. Rudnick, R.L.; Gao, S. Composition of the Continental Crust. In *Treatise on Geochemistry*; Elsevier: Amsterdam, The Netherlands, 2003; Volume 3, pp. 1–64.
3. Taylor, S.R.; McLennan, S.M. The Geochemical Evolution of the Continental Crust. *Rev. Geophys.* **1995**, *33*, 241–265. [[CrossRef](#)]

4. Kemp, A.I.S.; Hawkesworth, C.J.; Foster, G.L.; Paterson, B.A.; Woodhead, J.D.; Hergt, J.M.; Gray, C.M.; Whitehouse, M.J. Magmatic and Crustal Differentiation History of Granitic Rocks from Hf-O Isotopes in Zircon. *Science* **2007**, *315*, 980–983. [[CrossRef](#)]
5. Barbarin, B. A Review of the Relationships between Granitoid Types, Their Origins and Their Geodynamic Environments. *Lithos* **1999**, *46*, 605–626. [[CrossRef](#)]
6. Brown, M. Granite: From Genesis to Emplacement. *Bull. Geol. Soc. Am.* **2013**, *125*, 1079–1113. [[CrossRef](#)]
7. Chappell, B.W.; White, A.J.R. I- and S-Type Granites in the Lachlan Fold Belt. *Earth Environ. Sci. Trans. R. Soc. Edinb.* **1992**, *83*, 1–26. [[CrossRef](#)]
8. Hawkesworth, C.J.; Kemp, A.I.S. Using Hafnium and Oxygen Isotopes in Zircons to Unravel the Record of Crustal Evolution. *Chem. Geol.* **2006**, *226*, 144–162. [[CrossRef](#)]
9. Iles, K.A.; Hergt, J.M.; Woodhead, J.D.; Ickert, R.B.; Williams, I.S. Petrogenesis of Granitoids from the Lachlan Fold Belt, Southeastern Australia: The Role of Disequilibrium Melting. *Gondwana Res.* **2020**, *79*, 87–109. [[CrossRef](#)]
10. Jacob, J.-B.; Moyen, J.-F.; Fiannacca, P.; Laurent, O.; Bachmann, O.; Janoušek, V.; Farina, F.; Villaros, A. Crustal Melting vs. Fractionation of Basaltic Magmas: Part 2, Attempting to Quantify Mantle and Crustal Contributions in Granitoids. *Lithos* **2021**, *402–403*, 106292. [[CrossRef](#)]
11. Moyen, J.-F.; Janoušek, V.; Laurent, O.; Bachmann, O.; Jacob, J.-B.; Farina, F.; Fiannacca, P.; Villaros, A. Crustal Melting vs. Fractionation of Basaltic Magmas: Part 1, Granites and Paradigms. *Lithos* **2021**, *402–403*, 106291. [[CrossRef](#)]
12. Vigneresse, J.L. A New Paradigm for Granite Generation. *Earth Environ. Sci. Trans. R. Soc. Edinb.* **2004**, *95*, 11–22. [[CrossRef](#)]
13. Sawyer, E.W.; Cesare, B.; Brown, M. When the Continental Crust Melts. *Elements* **2011**, *7*, 229–234. [[CrossRef](#)]
14. Hawkesworth, C.; Cawood, P.; Kemp, T.; Storey, C.; Dhuime, B. A Matter of Preservation. *Science* **2009**, *323*, 49–50. [[CrossRef](#)]
15. Cawood, P.A.; Chowdhury, P.; Mulder, J.A.; Hawkesworth, C.J.; Capitanio, F.A.; Gunawardana, P.M.; Nebel, O. Secular Evolution of Continents and the Earth System. *Rev. Geophys.* **2022**, *60*, e2022RG000789. [[CrossRef](#)]
16. Laurent, O.; Martin, H.; Moyen, J.F.; Doucelance, R. The Diversity and Evolution of Late-Archean Granitoids: Evidence for the Onset of “Modern-Style” Plate Tectonics between 3.0 and 2.5 Ga. *Lithos* **2014**, *205*, 208–235. [[CrossRef](#)]
17. Condie, K.C.; Pisarevsky, S.A.; Puetz, S.J.; Roberts, N.M.W.; Spencer, C.J. A-Type Granites in Space and Time: Relationship to the Supercontinent Cycle and Mantle Events. *Earth Planet Sci. Lett.* **2023**, *610*, 118125. [[CrossRef](#)]
18. Bonin, B.; Janoušek, V.; Moyen, J.-F. Chemical Variation, Modal Composition and Classification of Granitoids. *Geol. Soc. Lond. Spec. Publ.* **2020**, *491*, 9–51. [[CrossRef](#)]
19. Frost, B.R.; Barnes, C.G.; Collins, W.J.; Arculus, R.J.; Ellis, D.J.; Frost, C.D. A Geochemical Classification for Granitic Rocks. *J. Petrol.* **2001**, *42*, 2033–2048. [[CrossRef](#)]
20. Gao, P.; Zheng, Y.; Zhao, Z. Experimental Melts from Crustal Rocks: A Lithochemical Constraint on Granite Petrogenesis. *Lithos* **2016**, *266–267*, 133–157. [[CrossRef](#)]
21. Loiselle, M.C.; Wones, D.R. Characteristics and Origin of Anorogenic Granites. *Geol. Soc. Am. Abstr. Program* **1979**, *11*, 468.
22. Frost, C.D.; Frost, B.R. On Ferroan (A-Type) Granitoids: Their Compositional Variability and Modes of Origin. *J. Petrol.* **2011**, *52*, 39–53. [[CrossRef](#)]
23. Bonin, B. A-Type Granites and Related Rocks: Evolution of a Concept, Problems and Prospects. *Lithos* **2007**, *97*, 1–29. [[CrossRef](#)]
24. Johansson, Å. A Tentative Model for the Origin of A-Type Granitoids. *Minerals* **2023**, *13*, 236. [[CrossRef](#)]
25. Collins, W.J.; Huang, H.-Q.; Bowden, P.; Kemp, A.I.S. Repeated S–I–A-Type Granite Trilogy in the Lachlan Orogen and Geochemical Contrasts with A-Type Granites in Nigeria: Implications for Petrogenesis and Tectonic Discrimination. *Geol. Soc. Lond. Spec. Publ.* **2020**, *491*, 53–76. [[CrossRef](#)]
26. Collins, W.J.; Beams, S.D.; White, A.J.R.; Chappell, B.W. Nature and Origin of A-Type Granites with Particular Reference to Southeastern Australia. *Contrib. Miner. Petrol.* **1982**, *80*, 189–200. [[CrossRef](#)]
27. Creaser, R.A.; Price, R.C.; Wormald, R.J. A-Type Granites Revisited: Assessment of a Residual-Source Model. *Geology* **1991**, *19*, 163–166. [[CrossRef](#)]
28. Eby, G.N. The A-Type Granitoids: A Review of Their Occurrence and Chemical Characteristics and Speculations on Their Petrogenesis. *Lithos* **1990**, *26*, 115–134. [[CrossRef](#)]
29. Dall’Agnol, R.; de Oliveira, D.C. Oxidized, Magnetite-Series, Rapakivi-Type Granites of Carajás, Brazil: Implications for Classification and Petrogenesis of A-Type Granites. *Lithos* **2007**, *93*, 215–233. [[CrossRef](#)]
30. King, P.L.; White, A.J.R.; Chappell, B.W.; Allen, C.M. Characterization and Origin of Aluminous A-Type Granites from the Lachlan Fold Belt, Southeastern Australia. *J. Petrol.* **1997**, *38*, 371–391. [[CrossRef](#)]
31. Sylvester, P.J. *Post-Collisional Strongly Peraluminous Granites*; Elsevier: Amsterdam, The Netherlands, 1998; Volume 45.
32. Ferré, E.C.; Caby, R.; Peucat, J.J.; Capdevila, R.; Monié, P. Pan-African, Post-Collisional, Ferro-Potassic Granite and Quartz–Monzonite Plutons of Eastern Nigeria. *Lithos* **1998**, *45*, 255–279. [[CrossRef](#)]
33. Goodenough, K.M.; Lusty, P.A.J.; Roberts, N.M.W.; Key, R.M.; Garba, A. Post-Collisional Pan-African Granitoids and Rare Metal Pegmatites in Western Nigeria: Age, Petrogenesis, and the ‘Pegmatite Conundrum’. *Lithos* **2014**, *200–201*, 22–34. [[CrossRef](#)]
34. Eby, G.N. Chemical Subdivision of the A-Type Granitoids: Petrogenetic and Tectonic Implications. *Geology* **1992**, *20*, 641. [[CrossRef](#)]
35. Amorim, J.V.A.d.; de Pinho Guimarães, I.; Farias, D.J.S.; Lima, J.V.d.; Santos, L.; Ribeiro, V.B.; Brainer, C. Late-Neoproterozoic Ferroan Granitoids of the Transversal Subprovince, Borborema Province, NE Brazil: Petrogenesis and Geodynamic Implications. *Int. Geol. Rev.* **2019**, *61*, 1745–1767. [[CrossRef](#)]

36. Almeida, C.N.; Guimarães, I.P.; Silva Filho, A.F. A-Type Post-Collisional Granites in the Borborema Province—NE Brazil: The Queimadas Pluton. *Gondwana Res.* **2002**, *5*, 667–681. [[CrossRef](#)]
37. Guimarães, I.P.; Silva Filho, A.F.; Melo, S.C.; Macambira, M.B. Petrogenesis of A-Type Granitoids from the Alto Moxoto and Alto Pajeu Terranes of the Borborema Province, Ne Brazil: Constraints from Geochemistry and Isotopic Composition. *Gondwana Res.* **2005**, *8*, 347–362. [[CrossRef](#)]
38. Lima, J.V.; Guimarães, I.d.P.; Santos, L.; Amorim, J.V.A.; Farias, D.J.S. Geochemical and Isotopic Characterization of the Granitic Magmatism along the Remígio—Pocinhos Shear Zone, Borborema Province, NE Brazil. *J. S. Am. Earth Sci.* **2017**, *75*, 116–133. [[CrossRef](#)]
39. Lages, G.d.A.; Marinho, M.d.S.; Nascimento, M.A.L.d.; Medeiros, V.C.d.; Dantas, E.L. Geocronologia e Aspectos Estruturais e Petrológicos Do Pluton Bravo, Domínio Central Da Província Borborema, Nordeste Do Brasil: Um Granito Transalcalino Precoce No Estágio Pós-Colisional Da Orogênese Brasileira. *Braz. J. Geol.* **2016**, *46*, 41–61. [[CrossRef](#)]
40. Hollanda, M.H.B.M.; Archanjo, C.J.; Souza, L.C.; Armstrong, R.; Vasconcelos, P.M. Cambrian Mafic to Felsic Magmatism and Its Connections with Transcurrent Shear Zones of the Borborema Province (NE Brazil): Implications for the Late Assembly of the West Gondwana. *Precambrian Res.* **2010**, *178*, 1–14. [[CrossRef](#)]
41. Van Schmus, W.R.; de Brito Neves, B.B.; Hackspacher, P.; Babinski, M. U-Pb and Sm-Nd Geochronologic Studies of the Eastern Borborema Province, Northeastern Brazil: Initial Conclusions. *J. S. Am. Earth Sci.* **1995**, *8*, 267–288. [[CrossRef](#)]
42. Caxito, F.d.A.; Santos, L.C.M.d.L.; Ganade, C.E.; Bendaoud, A.; Fettous, E.-H.; Bouyo, M.H. Toward an Integrated Model of Geological Evolution for NE Brazil-NW Africa: The Borborema Province and Its Connections to the Trans-Saharan (Benino-Nigerian and Tuareg Shields) and Central African Orogens. *Braz. J. Geol.* **2020**, *50*. [[CrossRef](#)]
43. Van Schmus, W.R.; Oliveira, E.P.; Silva Filho, A.F.; Toteu, S.F.; Penaye, J.; Guimarães, I.P. Proterozoic Links between the Borborema Province, NE Brazil, and the Central African Fold Belt. *Geol. Soc. Lond. Spec. Publ.* **2008**, *294*, 69–99. [[CrossRef](#)]
44. Toteu, S.F.; Van Schmus, W.R.; Penaye, J.; Michard, A. New U-Pb and Sm-Nd Data from North-Central Cameroon and Its Bearing on the Pre-Pan African History of Central Africa. *Precambrian Res.* **2001**, *108*, 45–73. [[CrossRef](#)]
45. Van Schmus, W.R.; Kozuch, M.; Brito Neves, B.B. Precambrian History of the Zona Transversal of the Borborema Province, NE Brazil: Insights from Sm-Nd and U-Pb Geochronology. *J. S. Am. Earth Sci.* **2011**, *31*, 227–252. [[CrossRef](#)]
46. Ferreira, A.C.D.; Dantas, E.L.; Fuck, R.A.; Nedel, I.M. Arc Accretion and Crustal Reworking from Late Archean to Neoproterozoic in Northeast Brazil. *Sci. Rep.* **2020**, *10*, 7855. [[CrossRef](#)] [[PubMed](#)]
47. Lira Santos, L.C.M.; Lages, G.A.; Caxito, F.A.; Dantas, E.L.; Cawood, P.A.; Lima, H.M.; da Cruz Lima, F.J. Isotopic and Geochemical Constraints for a Paleoproterozoic Accretionary Orogen in the Borborema Province, NE Brazil: Implications for Reconstructing Nuna/Columbia. *Geosci. Front.* **2022**, *13*, 101167. [[CrossRef](#)]
48. Dantas, E.L.; Hackspacher, P.C.; Van Schmus, W.R.V.; Brito Neves, B.B. Archean Accretion in the Sao Jose Do Campeste Massif, Borborema Province, Northeast Brazil. *Rev. Bras. Geociências* **1998**, *28*, 221–228. [[CrossRef](#)]
49. Guimarães, I.P.; Van Schmus, W.R.; Brito Neves, B.B.; Bretas Bittar, S.M.; Silva Filho, A.F.; Armstrong, R. U-Pb Zircon Ages of Orthogneisses and Supracrustal Rocks of the Cariris Velhos Belt: Onset of Neoproterozoic Rifting in the Borborema Province, NE Brazil. *Precambrian Res.* **2012**, *192–195*, 52–77. [[CrossRef](#)]
50. Neves, S.P. Constraints from Zircon Geochronology on the Tectonic Evolution of the Borborema Province (NE Brazil): Widespread Intracontinental Neoproterozoic Reworking of a Paleoproterozoic Accretionary Orogen. *J. S. Am. Earth Sci.* **2015**, *58*, 150–164. [[CrossRef](#)]
51. Hollanda, M.H.B.M.; Archanjo, C.J.; Bautista, J.R.; Souza, L.C. Detrital Zircon Ages and Nd Isotope Compositions of the Seridó and Lavras Da Mangabeira Basins (Borborema Province, NE Brazil): Evidence for Exhumation and Recycling Associated with a Major Shift in Sedimentary Provenance. *Precambrian Res.* **2015**, *258*, 186–207. [[CrossRef](#)]
52. Oliveira, E.P.; McNaughton, N.J.; Windley, B.F.; Carvalho, M.J.; Nascimento, R.S. Detrital Zircon U-Pb Geochronology and Whole-Rock Nd-Isotope Constraints on Sediment Provenance in the Neoproterozoic Sergipano Orogen, Brazil: From Early Passive Margins to Late Foreland Basins. *Tectonophysics* **2015**, *662*, 183–194. [[CrossRef](#)]
53. Araujo, C.E.G.; Cordani, U.G.; Basei, M.A.S.; Castro, N.A.; Sato, K.; Sproesser, W.M. U-Pb Detrital Zircon Provenance of Metasedimentary Rocks from the Ceará Central and Médio Coreaú Domains, Borborema Province, NE-Brazil: Tectonic Implications for a Long-Lived Neoproterozoic Active Continental Margin. *Precambrian Res.* **2012**, *206–207*, 36–51. [[CrossRef](#)]
54. Santos, T.J.S.; Fetter, A.H.; Hackspacher, P.C.; Van Schmus, W.R.; Nogueira Neto, J.A. Neoproterozoic Tectonic and Magmatic Episodes in the NW Sector of Borborema Province, NE Brazil, during Assembly of Western Gondwana. *J. S. Am. Earth Sci.* **2008**, *25*, 271–284. [[CrossRef](#)]
55. Sial, A.N.; Ferreira, V.P. Magma Associations in Ediacaran Granitoids of the Cachoeirinha–Salgueiro and Alto Pajeú Terranes, Northeastern Brazil: Forty Years of Studies. *J. S. Am. Earth Sci.* **2016**, *68*, 113–133. [[CrossRef](#)]
56. Oliveira, E.P.; Bueno, J.F.; McNaughton, N.J.; Silva Filho, A.F.; Nascimento, R.S.; Donatti-Filho, J.P. Age, Composition, and Source of Continental Arc- and Syn-Collision Granites of the Neoproterozoic Sergipano Belt, Southern Borborema Province, Brazil. *J. S. Am. Earth Sci.* **2015**, *58*, 257–280. [[CrossRef](#)]
57. Nascimento, M.A.L.; Galindo, A.C.; Medeiros, V.C. Ediacaran to Cambrian Magmatic Suites in the Rio Grande Do Norte Domain, Extreme Northeastern Borborema Province (NE of Brazil): Current Knowledge. *J. S. Am. Earth Sci.* **2015**, *58*, 281–299. [[CrossRef](#)]

58. Guimarães, I.P.; Silva Filho, A.F.; Almeida, C.N.; Van Schmus, W.R.; Araújo, J.M.M.; Melo, S.C.; Melo, E.B. Brasiliano (Pan-African) Granitic Magmatism in the Pajeú-Paraíba Belt, Northeast Brazil: An Isotopic and Geochronological Approach. *Precambrian Res.* **2004**, *135*, 23–53. [[CrossRef](#)]
59. Silva Filho, A.F.; Guimarães, I.d.P.; Santos, L.; Armstrong, R.; Van Schmus, W.R. Geochemistry, U–Pb Geochronology, Sm–Nd and O Isotopes of ca. 50 Ma Long Ediacaran High-K Syn-Collisional Magmatism in the Pernambuco Alagoas Domain, Borborema Province, NE Brazil. *J. S. Am. Earth Sci.* **2016**, *68*, 134–154. [[CrossRef](#)]
60. Ferreira, V.P.; Silva, T.R.d.; Lima, M.M.C.d.; Sial, A.N.; Silva Filho, A.F.; Neves, C.H.F.S.; Tchouankoue, J.P.; Lima, S.S. Tracing a Neoproterozoic Subduction to Collision Magmatism in the Eastern Pernambuco–Alagoas Domain, Northeastern Brazil. *J. S. Am. Earth Sci.* **2023**, *128*, 104457. [[CrossRef](#)]
61. Neves, S.P.; Tommasi, A.; Vauchez, A.; Carrino, T.A. The Borborema Strike-Slip Shear Zone System (NE Brazil): Large-Scale Intracontinental Strain Localization in a Heterogeneous Plate. *Lithosphere* **2021**, *2021*, 6407232. [[CrossRef](#)]
62. Caby, R. *Precambrian Terranes of Benin-Nigeria and Northeast Brazil and the Late Proterozoic South Atlantic Fit*; Terranes in the Circum-Atlantic Paleozoic Orogens: Boulder, CO, USA, 1989; pp. 145–158.
63. Vauchez, A.; Neves, S.P.; Caby, R.; Corsini, M.; Egydio-Silva, M.; Arthaud, M.; Amaro, V. The Borborema Shear Zone System, NE Brazil. *J. S. Am. Earth Sci.* **1995**, *8*, 247–266. [[CrossRef](#)]
64. Araujo, C.E.G.; Weinberg, R.F.; Caxito, F.A.; Lopes, L.B.L.; Tesser, L.R.; Costa, I.S. Decratonization by Rifting Enables Orogenic Reworking and Transcurrent Dispersal of Old Terranes in NE Brazil. *Sci. Rep.* **2021**, *11*, 5719. [[CrossRef](#)]
65. Archanjo, C.J.; Hollanda, M.H.B.M.; Rodrigues, S.W.O.; Brito Neves, B.B.B.; Armstrong, R. Fabrics of Pre- and Syntectonic Granite Plutons and Chronology of Shear Zones in the Eastern Borborema Province, NE Brazil. *J. Struct. Geol.* **2008**, *30*, 310–326. [[CrossRef](#)]
66. Santos, L.C.M.d.L.; Dantas, E.L.; Cawood, P.A.; Lages, G.d.A.; Lima, H.M.; dos Santos, E.J.; Caxito, F.A. Early to Late Neoproterozoic Subduction-Accretion Episodes in the Cariris Velhos Belt of the Borborema Province, Brazil: Insights from Isotope and Whole-Rock Geochemical Data of Supracrustal and Granitic Rocks. *J. S. Am. Earth Sci.* **2019**, *96*, 102384. [[CrossRef](#)]
67. Santos, L.C.M.d.L.; Dantas, E.L.; Cawood, P.A.; Lages, G.d.A.; Lima, H.M.; dos Santos, E.J. The Cariris Velhos Tectonic Event in Northeast Brazil. *J. S. Am. Earth Sci.* **2010**, *29*, 61–76. [[CrossRef](#)]
68. Lira Santos, L.C.M.; Dantas, E.L.; Cawood, P.A.; Lages, G.d.A.; Lima, H.M.; Santos, E.J. Accretion Tectonics in Western Gondwana Deduced From Sm–Nd Isotope Mapping of Terranes in the Borborema Province, NE Brazil. *Tectonics* **2018**, *37*, 2727–2743. [[CrossRef](#)]
69. Santos, L.C.M.D.L.; de Oliveira, R.G.; Lages, G.d.A.; Dantas, E.L.; Caxito, F.; Cawood, P.A.; Fuck, R.A.; Lima, H.M.; Santos, G.L.; Neto, J.F.d.A. Evidence for Neoproterozoic Terrane Accretion in the Central Borborema Province, West Gondwana Deduced by Isotopic and Geophysical Data Compilation. *Int. Geol. Rev.* **2022**, *64*, 1574–1593. [[CrossRef](#)]
70. Brito Neves, B.B.; Santos, E.J.d.; Fuck, R.A.; Santos, L.C.M.L. A Preserved Early Ediacaran Magmatic Arc at the Northernmost Portion of the Transversal Zone Central Subprovince of the Borborema Province, Northeastern South America. *Braz. J. Geol.* **2016**, *46*, 491–508. [[CrossRef](#)]
71. Neves, S.P. Proterozoic History of the Borborema Province (NE Brazil): Correlations with Neighboring Cratons and Pan-African Belts and Implications for the Evolution of Western Gondwana. *Tectonics* **2003**, *22*. [[CrossRef](#)]
72. Mariano, G.; Neves, S.P.; Siva Filho, A.F.; Guimaraes, I.P. Diorites of the High-K Calc-Alkalic Association: Geochemistry and Sm–Nd Data and Implications for the Evolution of the Borborema Province, Northeast Brazil. *Int. Geol. Rev.* **2001**, *43*, 921–929. [[CrossRef](#)]
73. Lima, J.V.d.; Guimarães, I.d.P.; Neves, S.P.; Basei, M.A.S.; Silva Filho, A.F.; Brainer, C.C.G. Post-Collisional, High-Ba–Sr Teixeira Batholith Granites: Evidence for Recycling of Paleoproterozoic Crust in the Alto Pajeú Domain, Borborema Province—NE-Brazil. *Lithos* **2021**, *404–405*, 106469. [[CrossRef](#)]
74. Hollanda, M.H.B.M.; Pimentel, M.M.; Jardim de Sá, E.F. Paleoproterozoic Subduction-Related Metasomatic Signatures in the Lithospheric Mantle beneath NE Brazil: Inferences from Trace Element and Sr–Nd–Pb Isotopic Compositions of Neoproterozoic High-K Igneous Rocks. *J. S. Am. Earth Sci.* **2003**, *15*, 885–900. [[CrossRef](#)]
75. Neves, S.P.; Bruguier, O.; Vauchez, A.; Bosch, D.; Silva, J.M.R.d.; Mariano, G. Timing of Crust Formation, Deposition of Supracrustal Sequences, and Transamazonian and Brasiliano Metamorphism in the East Pernambuco Belt (Borborema Province, NE Brazil): Implications for Western Gondwana Assembly. *Precambrian Res.* **2006**, *149*, 197–216. [[CrossRef](#)]
76. Santos, T.J.S.; Fetter, A.H.; Neto, J.A.N. Comparisons between the Northwestern Borborema Province, NE Brazil, and the Southwestern Pharusian Dahomey Belt, SW Central Africa. *Geol. Soc. Lond. Spec. Publ.* **2008**, *294*, 101–120. [[CrossRef](#)]
77. Araújo, M.N.C.; Vasconcelos, P.M.; Alves da Silva, F.C.; Jardim de Sá, E.F.; Sá, J.M. ⁴⁰Ar/³⁹Ar Geochronology of Gold Mineralization in Brasiliano Strike-Slip Shear Zones in the Borborema Province, NE Brazil. *J. S. Am. Earth Sci.* **2005**, *19*, 445–460. [[CrossRef](#)]
78. Araújo Neto, J.F.d.; Santos, L.C.M.d.L.; Viegas, G.; Souza, C.P.d.; Miggins, D.; Cawood, P.A. Structural and Geochronological Constraints on the Portalegre Shear Zone: Implications for Emerald Mineralization in the Borborema Province, Brazil. *J. Struct. Geol.* **2023**, *174*, 104921. [[CrossRef](#)]
79. Lira Santos, L.C.M.; Dantas, E.L.; Cawood, P.A.; José dos Santos, E.; Fuck, R.A. Neoproterozoic Crustal Growth and Paleoproterozoic Reworking in the Borborema Province, NE Brazil: Insights from Geochemical and Isotopic Data of TTG and Metagranitic Rocks of the Alto Moxotó Terrane. *J. S. Am. Earth Sci.* **2017**, *79*, 342–363. [[CrossRef](#)]

80. Santos, L.; Guimarães, I.P.; Silva Filho, A.F.; Farias, D.J.S.; Lima, J.V.; Antunes, J. V Magmatismo Ediacarano Extensional Na Província Borborema, NE Brasil: Pluton Serra Branca. *Comun. Geológicas* **2014**, *101*, 199–203.
81. Miranda, A.W.A. Evolução Estrutural das zonas de Cisalhamento Dúcteis na Porção Centro-Leste do Domínio da Zona Transversal na Província Borborema. Ph.D. Thesis, Universidade do Estado do Rio de Janeiro, Rio de Janeiro, Brazil, 2010.
82. Guimarães, I.P.; Silva Filho, A.F.; Lima, J.V.; Farias, D.J.S.; Amorim, J.V.A.; Silva, F.M.J. V Geocronologia U-Pb e Caracterização Geoquímica Dos Granitoides Do Pluton Marinho, Província Borborema. In Proceedings of the 46^o Congresso Brasileiro de Geologia Anais Proceedings, Santos, Brazil, 5 October 2012.
83. Silva, J.M.R.D.; Mariano, G. Geometry and Kinematics of the Afogados Da Ingazeira Shear Zone, Northeast Brazil. *Int. Geol. Rev.* **2000**, *42*, 86–95. [[CrossRef](#)]
84. Melo, E.B. de Petrologia e Geoquímica de Granitoides a Sudeste da zona de Cisalhamento Afogados da Ingazeira—PE Nordeste do Brasil. Ph.D. Thesis, Universidade Federal de Pernambuco, Recife, Brazil, 2004.
85. Ishihara, S. The Magnetite-Series and Ilmenite-Series Granitic Rocks. *Min. Geol.* **1977**, *27*, 293–305.
86. Pearce, J.A.; Harris, N.B.W.; Tindle, A.G. Trace Element Discrimination Diagrams for the Tectonic Interpretation of Granitic Rocks. *J. Petrol.* **1984**, *25*, 956–983. [[CrossRef](#)]
87. Whalen, J.B.; Currie, K.L.; Chappell, B.W. A-Type Granites: Geochemical Characteristics, Discrimination and Petrogenesis. *Contrib. Miner. Petrol.* **1987**, *95*, 407–419. [[CrossRef](#)]
88. Lima, J.V.d.; Guimaraes, I.D.P.; Santos, L.; Farias, D.J.; Antunes, J.V. Química Mineral e Condições de Cristalização de Granitos Intrudidos Ao Longo Da Zona de Cisalhamento Remígio—Pocinhos, NE Do Brasil: Plúton Pilõezinhos. *Pesqui. Em Geociências* **2017**, *44*, 123. [[CrossRef](#)]
89. Santos, L.; Guimaraes, I.P.; Farias, D.J.S.; Lima, J. V Geologia, petrografia e química mineral de plutons contrastantes, Serra Branca e Coxixola, ao longo da Zona de Cisalhamento Coxixola, Província Borborema, NE Brasil. *Estud. Geológicos* **2013**, *23*, 111–142.
90. Locock, A.J. An Excel Spreadsheet to Classify Chemical Analyses of Amphiboles Following the IMA 2012 Recommendations. *Comput. Geosci.* **2014**, *62*, 1–11. [[CrossRef](#)]
91. Hawthorne, F.C.; Oberti, R.; Harlow, G.E.; Maresch, W.V.; Martin, R.F.; Schumacher, J.C.; Welch, M.D. Nomenclature of the Amphibole Supergroup. *Am. Miner.* **2012**, *97*, 2031–2048. [[CrossRef](#)]
92. Czamanske, G.K.; Wones, D.R. Oxidation During Magmatic Differentiation, Finnmarka Complex, Oslo Area, Norway: Part 2, The Mafic Silicates1. *J. Petrol.* **1973**, *14*, 349–380. [[CrossRef](#)]
93. Foster, M.D. Interpretation of the Composition of Trioctahedral Micas. *US Geol. Surv. Prof. Pap. B* **1960**, *354*, 1–49.
94. Gündüz, M.; Asan, K. MagMin_PT: An Excel-based mineral classification and geothermobarometry program for magmatic rocks. *Mineral. Mag.* **2023**, *87*, 1–9. [[CrossRef](#)]
95. Speer, J.A. Micas in Igneous Rocks. In *Micas*; Bailey, S.W., Ed.; De Gruyter: Berlin, Germany, 1984; Volume 13, pp. 299–356.
96. Nachit, H.; Razafimahefa, N.; Stussi, J.-M.; Carron, J.-P. Composition Chimique Des Biotites et Typologie Magmatique Des Granitoides. *Comptes Rendus Hebd. De L'academie Des Sci.* **1985**, *301*, 813–818.
97. Abdel-Rahman, A.-F.M. Nature of Biotites from Alkaline, Calc-Alkaline, and Peraluminous Magmas. *J. Petrol.* **1994**, *35*, 525–541. [[CrossRef](#)]
98. Deer, W.A.; Howie, R.; Zussman, J. *An Introduction to the Rock—Forming Minerals*, 2nd ed.; Pearson Education Limited: London, UK, 1992; pp. 1–712.
99. Jochum, K.P.; Weis, U.; Stoll, B.; Kuzmin, D.; Yang, Q.; Raczek, I.; Jacob, D.E.; Stracke, A.; Birbaum, K.; Frick, D.A.; et al. Determination of Reference Values for NIST SRM 610-617 Glasses Following ISO Guidelines. *Geostand. Geoanalyt. Res.* **2011**, *35*, 397–429. [[CrossRef](#)]
100. Van Achterbergh, E.; Ryan, C.G.; Jackson, S.E.; Griffin, W.L. Data Reduction Software for LA-ICP-MS. In *Laser-Ablation-ICPMS in the Earth Sciences; Principles and Applications*; Sylvester, P.J., Ed.; Mineralogical Association of Canada: Ottawa, ON, Canada, 2001; pp. 239–243.
101. Burnham, A.D. Key Concepts in Interpreting the Concentrations of the Rare Earth Elements in Zircon. *Chem. Geol.* **2020**, *551*, 119765. [[CrossRef](#)]
102. El-Bialy, M.Z.; Ali, K.A. Zircon Trace Element Geochemical Constraints on the Evolution of the Ediacaran (600–614Ma) Post-Collisional Dokhan Volcanics and Younger Granites of SE Sinai, NE Arabian-Nubian Shield. *Chem. Geol.* **2013**, *360–361*, 54–73. [[CrossRef](#)]
103. Rubatto, D. Zircon Trace Element Geochemistry: Partitioning with Garnet and the Link between U-Pb Ages and Metamorphism. *Chem. Geol.* **2002**, *184*, 123–138. [[CrossRef](#)]
104. Hoskin, P.W.O.; Schaltegger, U. The Composition of Zircon and Igneous and Metamorphic Petrogenesis. *Rev. Miner. Geochem.* **2003**, *53*, 27–62. [[CrossRef](#)]
105. Pupin, J.P. Zircon and Granite Petrology. *Contrib. Miner. Petrol.* **1980**, *73*, 207–220. [[CrossRef](#)]
106. Harley, S.L.; Kelly, N.M. Zircon Tiny but Timely. *Elements* **2007**, *3*, 13–18. [[CrossRef](#)]
107. Smythe, D.J.; Brenan, J.M. Magmatic Oxygen Fugacity Estimated Using Zircon-Melt Partitioning of Cerium. *Earth Planet Sci. Lett.* **2016**, *453*, 260–266. [[CrossRef](#)]
108. Valley, J.W. Oxygen Isotopes in Zircon. *Rev. Miner. Geochem.* **2003**, *53*, 343–385. [[CrossRef](#)]
109. Kirkland, C.L.; Smithies, R.H.; Taylor, R.J.M.; Evans, N.; McDonald, B. Zircon Th/U Ratios in Magmatic Environs. *Lithos* **2015**, *212–215*, 397–414. [[CrossRef](#)]

110. Trail, D.; Watson, E.B.; Tailby, N.D. Ce and Eu Anomalies in Zircon as Proxies for the Oxidation State of Magmas. *Geochim. Cosmochim. Acta* **2012**, *97*, 70–87. [[CrossRef](#)]
111. Schiller, D.; Finger, F. Application of Ti-in-Zircon Thermometry to Granite Studies: Problems and Possible Solutions. *Contrib. Miner. Petrol.* **2019**, *174*, 51. [[CrossRef](#)] [[PubMed](#)]
112. Loucks, R.R.; Henriques, G.J.; Fiorentini, M.L. Zircon and Whole-Rock Trace Element Indicators of Magmatic Hydration State and Oxidation State Discriminate Copper Ore-Forming from Barren Arc Magmas. *Econ. Geol.* **2024**, *119*, 511–523. [[CrossRef](#)]
113. Schaltegger, U. Hydrothermal Zircon. *Elements* **2007**, *203*, 183–203. [[CrossRef](#)]
114. Fu, B.; Mernagh, T.P.; Kita, N.T.; Kemp, A.I.S.; Valley, J.W. Distinguishing Magmatic Zircon from Hydrothermal Zircon: A Case Study from the Gidginbung High-Sulphidation Au-Ag-(Cu) Deposit, SE Australia. *Chem. Geol.* **2009**, *259*, 131–142. [[CrossRef](#)]
115. Hoskin, P.W.O. Trace-Element Composition of Hydrothermal Zircon and the Alteration of Hadean Zircon from the Jack Hills, Australia. *Geochim. Cosmochim. Acta* **2005**, *69*, 637–648. [[CrossRef](#)]
116. Williams, I.S.; Claesson, S. Isotopic Evidence for the Precambrian Provenance and Caledonian Metamorphism of High Grade Paragneisses from the Seve Nappes, Scandinavian Caledonides. *Contrib. Miner. Petrol.* **1987**, *97*, 205–217. [[CrossRef](#)]
117. Taylor, S.R.; McLennan, S.H. *The Continental Crust: Its Composition and Evolution*; Blackwell Scientific: Oxford, UK, 1985.
118. Breiter, K.; Lamarão, C.N.; Borges, R.M.K.; Dall’Agnol, R. Chemical Characteristics of Zircon from A-Type Granites and Comparison to Zircon of S-Type Granites. *Lithos* **2014**, *192–195*, 208–225. [[CrossRef](#)]
119. Xie, L.; Wang, R.; Chen, X.; Qiu, J.; Wang, D. Th-Rich Zircon from Peralkali Line A-Type Granite: Mineralogical Features and Petrological Implications. *Chin. Sci. Bull.* **2005**, *50*, 809–817. [[CrossRef](#)]
120. Santos, L. Caracterização petrológica e geoquímica dos granitoides intrudidos ao longo da zona de cisalhamento Coxixola, Província Borborema, NE Brasil: Plutons Serra Branca e Coxixola. Master’s Thesis, Universidade Federal de Pernambuco, Recife, Brazil, 2013.
121. Vilalva, F.C.J.; Simonetti, A.; Vlach, S.R.F. Insights on the Origin of the Graciosa A-Type Granites and Syenites (Southern Brazil) from Zircon U-Pb Geochronology, Chemistry, and Hf and O Isotope Compositions. *Lithos* **2019**, *340–341*, 20–33. [[CrossRef](#)]
122. Loucks, R.R.; Fiorentini, M.L.; Henriques, G.J. New Magmatic Oxybarometer Using Trace Elements in Zircon. *J. Petrol.* **2020**, *61*, ega034. [[CrossRef](#)]
123. Blundy, J.D.; Holland, T.J.B. Calcic Amphibole Equilibria and a New Amphibole-Plagioclase Geothermometer. *Contrib. Miner. Petrol.* **1990**, *104*, 208–224. [[CrossRef](#)]
124. Ridolfi, F.; Renzulli, A.; Puerini, M. Stability and Chemical Equilibrium of Amphibole in Calc-Alkaline Magmas: An Overview, New Thermobarometric Formulations and Application to Subduction-Related Volcanoes. *Contrib. Miner. Petrol.* **2010**, *160*, 45–66. [[CrossRef](#)]
125. Ridolfi, F.; Renzulli, A. Calcic Amphiboles in Calc-Alkaline and Alkaline Magmas: Thermobarometric and Chemometric Empirical Equations Valid up to 1130 °C and 2.2 GPa. *Contrib. Miner. Petrol.* **2012**, *163*, 877–895. [[CrossRef](#)]
126. Putirka, K. Amphibole Thermometers and Barometers for Igneous Systems and Some Implications for Eruption Mechanisms of Felsic Magmas at Arc Volcanoes. *Am. Miner.* **2016**, *101*, 841–858. [[CrossRef](#)]
127. Watson, E.B.; Wark, D.A.; Thomas, J.B. Crystallization Thermometers for Zircon and Rutile. *Contrib. Miner. Petrol.* **2006**, *151*, 413–433. [[CrossRef](#)]
128. Boehnke, P.; Watson, E.B.; Trail, D.; Harrison, T.M.; Schmitt, A.K. Zircon Saturation Re-Revisited. *Chem. Geol.* **2013**, *351*, 324–334. [[CrossRef](#)]
129. Watson, E.B.; Harrison, T.M. Zircon Saturation Revisited: Temperature and Composition Effects in a Variety of Crustal Magma Types. *Earth Planet Sci. Lett.* **1983**, *64*, 295–304. [[CrossRef](#)]
130. Harrison, T.M.; Watson, E.B. The Behavior of Apatite during Crustal Anatexis: Equilibrium and Kinetic Considerations. *Geochim. Cosmochim. Acta* **1984**, *48*, 1467–1477. [[CrossRef](#)]
131. Schmidt, M.W. Amphibole Composition in Tonalite as a Function of Pressure: An Experimental Calibration of the Al-in-Hornblende Barometer. *Contrib. Miner. Petrol.* **1992**, *110*, 304–310. [[CrossRef](#)]
132. Anderson, J.L.; Smith, D.R. The Effects of Temperature and FO₂ on the Al-in-Hornblende Barometer. *Am. Miner.* **1995**, *80*, 549–559. [[CrossRef](#)]
133. Hammarstrom, J.M.; Zen, E. Aluminum in Hornblende: An Empirical Igneous Geobarometer. *Am. Miner.* **1986**, *71*, 1297–1313.
134. Mutch, E.J.F.; Blundy, J.D.; Tattitch, B.C.; Cooper, F.J.; Brooker, R.A. An Experimental Study of Amphibole Stability in Low-Pressure Granitic Magmas and a Revised Al-in-Hornblende Geobarometer. *Contrib. Miner. Petrol.* **2016**, *171*, 85. [[CrossRef](#)]
135. Wones, D.R. Significance of the Assemblage Titanite+magnetite+quartz in Granitic Rocks. *Am. Miner.* **1989**, *74*, 744–749.
136. Frost, B.R.; Lindsley, D.H. Equilibria among Fe-Ti Oxides, Pyroxenes, Olivine, and Quartz: Part II. Application. *Am. Miner.* **1992**, *77*, 1004–1020.
137. Anderson, J.L.; Barth, A.P.; Wooden, J.L.; Mazdab, F. Thermometers and Thermobarometers in Granitic Systems. *Rev. Miner. Geochem.* **2008**, *69*, 121–142. [[CrossRef](#)]
138. Nardi, L.V.S.; Formoso, M.L.L.; Müller, I.F.; Fontana, E.; Jarvis, K.; Lamarão, C. Zircon/Rock Partition Coefficients of REEs, Y, Th, U, Nb, and Ta in Granitic Rocks: Uses for Provenance and Mineral Exploration Purposes. *Chem. Geol.* **2013**, *335*, 1–7. [[CrossRef](#)]

Disclaimer/Publisher’s Note: The statements, opinions and data contained in all publications are solely those of the individual author(s) and contributor(s) and not of MDPI and/or the editor(s). MDPI and/or the editor(s) disclaim responsibility for any injury to people or property resulting from any ideas, methods, instructions or products referred to in the content.